

AD-A149 059

CHINESE JOURNAL OF INFRARED RESEARCH (SELECTED
ARTICLES)(U) FOREIGN TECHNOLOGY DIV WRIGHT-PATTERSON
AFB OH H GONG ET AL. 09 FEB 83 FTD-ID(RS)T-1655-82

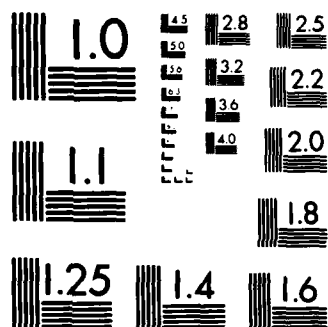
1/1

UNCLASSIFIED

F/G 17/5

NL

			END									
			FILED									
			DTG									



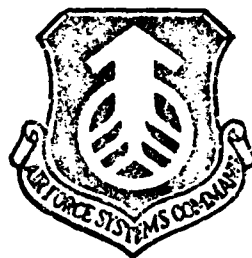
MICROCOPY RESOLUTION TEST CHART
NATIONAL BUREAU OF STANDARDS-1963-A

AD-A149 059

DIC FILE COPY

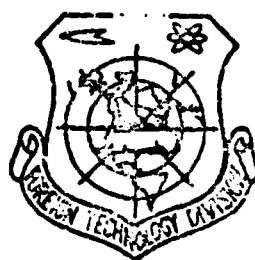
FTD-ID(RS)T-1655-82

FOREIGN TECHNOLOGY DIVISION



CHINESE JOURNAL OF INFRARED RESEARCH

(Selected Articles)



DIC
ELECTE
JAN 16 1985
S D D

Approved for public release;
distribution unlimited.

85 01 09 045

Accession For	
NTIS GRA&I	<input checked="" type="checkbox"/>
DTIC TAB	<input type="checkbox"/>
Unannounced	<input type="checkbox"/>
Justification	<input type="checkbox"/>
By	
Distribution/	
Availability Codes	
Dist	Avail and/or Special
AI	

FTD-ID(RS)T-1655-82

EDITED TRANSLATION



FTD-ID(RS)T-1655-82

9 February 1983

MICROFICHE NR: FTD-83-C-000175

CHINESE JOURNAL OF INFRARED RESEARCH (Selected Articles)

English pages: 33

Source: Hongwai Janjiu, Vol. 1, Nr. 2, 1982,
pp. 93-106; 145-148

Country of origin: China

Translated by: LEO KANNER ASSOCIATES
F33657-81-D-0264

Requester: FTD/WE

Approved for public release; distribution unlimited.

THIS TRANSLATION IS A RENDITION OF THE ORIGINAL FOREIGN TEXT WITHOUT ANY ANALYTICAL OR EDITORIAL COMMENT. STATEMENTS OR THEORIES ADVOCATED OR IMPLIED ARE THOSE OF THE SOURCE AND DO NOT NECESSARILY REFLECT THE POSITION OR OPINION OF THE FOREIGN TECHNOLOGY DIVISION.

PREPARED BY:

TRANSLATION DIVISION
FOREIGN TECHNOLOGY DIVISION
WPAFB, OHIO.

FTD-ID(RS)T-1655-82

Date 9 Feb 19 83

Table of Contents

Graphics Disclaimer	ii
Several Problems in Developing a Satellite-Borne Infrared Remote Sensor and Ways to Solve Them, by Gong Huixing	1
Infrared Remote Sensing of Over-Land Atmospheric Temperature Profiles from Satellite, by Zhao Goaxiang	14
A Method of Determining the Brightness Temperature in a Short Wave Infrared Atmospheric Spectral Window from Satellite Measurement, by Wang Qinmo	28

GRAPHICS DISCLAIMER

All figures, graphics, tables, equations, etc. merged into this translation were extracted from the best quality copy available.

SEVERAL PROBLEMS IN DEVELOPING A SATELLITE-BORNE INFRARED REMOTE SENSOR AND WAYS TO SOLVE THEM*

Gong Huixing

Shanghai Institute of Technical Physics, Chinese Academy of Sciences

Received 16 January 1982

Several specially-considered problems in developing a satellite-borne infrared remote sensor are discussed. These problems include: the definition of scanning period, the scanner and its lubrication in outer-space environment of very high vacuum, and infrared radiation calibration and so on. The ways to solve them are suggested.

In the recent decade, with the appearance of a long-service-life (free from power source) radiation cooler and tellurium-cadmium-mercury (TeCdHg) infrared detector with 77K~105K operating temperature, detection rate $D^* \geq 1 \times 10^{10} \text{ cm} \cdot \text{Hz}^{1/2} / \text{W}$, response time $\tau \leq 1 \text{ } \mu\text{s}$, and response wavelength $\lambda_0 \geq 14 \text{ } \mu\text{m}$, infrared remote sensors of optical mechanical scanning type were installed in a long-service-life operation meteorological satellite and land resources satellite to conduct periodic high discriminability observations of continents, atmosphere and oceans of the earth. Since the optical scanning multiband infrared remote sensor has the observation capability of the long wave infrared wide band, the sensor occupies an important position in space remote sensing.

*All comrades in Section #720 and #730 took part in the work.

Figure 1 shows a simplified light channel of a type of multiband scanner, including a scan reflective mirror, forming a 45° angle with the rotating shaft, which is in the same direction as satellite flight. When the scan mirror rotates, the instrument scans the direction perpendicular to the satellite flight, and receives radiation emission or reflection of the ground-atmosphere system by using a fixed optical instantaneous visual field. By taking advantage of the forward motion of the satellite's revolution around the earth, scenes of the atmosphere, continents and oceans can be obtained (Fig. 2).

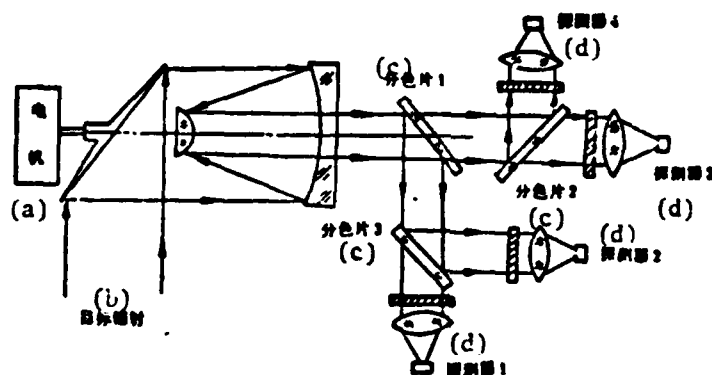


Fig. 1. Schematic diagram of light channel of TIROS-N AVHRR four-band infrared scanner.

Key: (a) Motor; (b) Target radiation; (c) Dispersion lens; (d) Detector.

This paper gives a brief discussion concerning problems and solution methods in the development of this type of remote sensor.

1. Determination of scanning speed

In order to maintain a constant scale (with respect to time and location) of the received scene photographs, the scanner requires that the satellite orbit be a circle. In that case, the moving speed of the satellite projection on the ground surface is:

$$V = \frac{R}{R+h} \sqrt{\frac{\mu}{R+h}}, \quad (1)$$

In the equation, R is the earth's radius; h is the orbit altitude; and the Kepler constant $\mu = 3.986 \times 10^5 \text{ km}^3/\text{s}^2$.

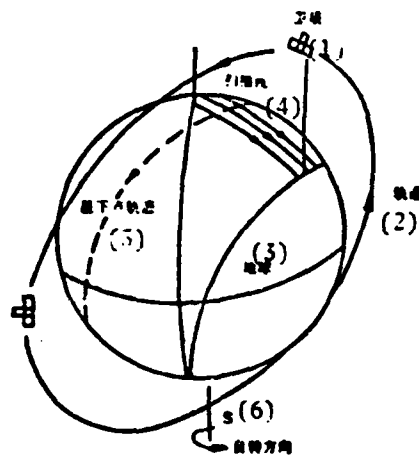


Fig. 2. Diagram showing the principle of photographing an earth scene by a scanner.

Key: (1) Satellite; (2) Orbit; (3) Earth; (4) Scanning lines; (5) Satellite projection locus; (6) Direction of earth's rotation.

If the latitude of the instantaneous visual field of a detector (of the instrument) is α along the satellite flight direction, in order to avoid misscanning of scenes on the ground surface, the scanning period T of the scanner should be:

$$T = \frac{N \cdot \alpha \cdot h(R+h)}{R} \sqrt{\frac{R+h}{\mu}}, \quad (2)$$

In the equation, N is the number of elements of the detector.

2. Requirements on orbit

In the radiation sounding of the infrared channel ($10.5\sim 12.5\mu\text{m}$) of an atmospheric spectral window, a TeCdMg detector is required; the detector is installed on a second-stage cold block of the two-stage radiation cooler with an operating temperature of 105K. In order to maintain sufficient exchange of heat radiation between the radiation cooler and the 3K cold space environment, the opening of the radiator should aim consistently at the cold space.

In a satellite with three-axis attitude stability with respect to the ground, the drift and rolling shafts of the satellite rotate around the pitch axis at the same angular velocity as the satellite's revolution around the earth. Since the pitch axis is perpendicular to the orbital plane, the axis is relatively stable in space. Hence, in the polar region and the synchronizing orbit of the earth, the opening of the radiation cooler is toward the shady direction, the same as the pitch axis. In order to avoid sunlight shining onto the opening of the radiation cooler, it is necessary to maintain generally a constant angle between the sunlight and the orbital plane of the satellite; this is the solar synchronizing orbit. The method of synchronizing with the sun is to control the launch dip angle i of the orbit. When i satisfies

$$i = \cos^{-1} \left[-0.0985(1-e^2)^2 \left(\frac{a}{R} \right)^{1.5} \right] \quad (3)$$

(e is the orbit eccentricity; and a is the semi-major axis of the orbit), the perturbation of the satellite's motion by the protruding mass of the equator can allow the rotation of the orbital plane around the earth's rotational axis to cancel the variation between the sunlight and the orbital plane because of the earth's revolution around the sun. In the synchronizing orbit around the sun, the annual variation of the intersecting angle between the sun and the orbital plane does not exceed $\pm 23.5^\circ$.

3. Drive device of scanning mirror

The earth-scene signals used for satellite photography can be converted into pictures through ground receiving stations by machine synchronization.

When satellite picture transmission uses a single channel simulated signal for output, the longterm and instantaneous stability of the rotational speed of the scanning mirror should be strictly controlled to avoid slanting and fluctuation of pictures received by the ground because the synchronized reference signals of rotational speed (of the scanning mirror) do not accompany the output signal.

In order to simplify the transmission structure, to solve the wearing and lubrication problems of the gears, and to increase service life and reliability, a TDB-500 low-speed permanent-magnetic-type ac synchronous motor is used to directly drive the 45° scanning mirror. The TDB-500 is the axial-direction exciting magnet, operating on the principle of varying gas gap magnetic conductance due to open slots of the stator and rotor. The rotational speed N of the rotor is:

$$N = 60 \times (\text{frequency of power source} / \text{number of open slots of the rotor}) \quad (4)$$

(rpm)

The number of open slots of the rotor is 50; when the frequency of the power source is 100 Hz, the motor rotational speed is 120 rpm. Since this is a synchronous motor, the average rotational speed of the rotor is determined by the frequency of the power source. By using a power source with quartz oscillation frequency division, a frequency stability of 3×10^{-6} can be attained. The motor operates on the speed reduction principle of an electromagnet with 50 times the specific synchronizing moment of an ordinary motor. Through measurement, the fluctuating angle of the scanning mirror is less than 0.8 mrad.

The greatest flaw in using a synchronous motor is that it is relatively complex in starting up because the greatest synchronizing angle is 1.8° for a motor with a speed reduction ratio of 50. When the rotational speed is 100 rpm, it is equivalent to starting up the rotor component with an inertia ($J = 1.8 \times 10^4 \text{ g} \cdot \text{cm}^2$) within a duration of 5 ms. Based on the relationship of the starting moment $M = 2 \cdot J(N/60)^2 \times \text{speed reduction ratio}$, the motor should have a moment of $7.2 \times 10^5 \text{ g} \cdot \text{cm}$, which considerably exceeds the moment output capacity of the TDB-500 motor. Hence, a variable frequency scheme is selected. Under

the situation of constant motor voltage of the power source, when the source frequency is reduced, the stator current increases and the starting moment rises; the inertia moment of the rotor decreases with the square law. Figure 3 shows that the motor's starting moment is equal to its inertia moment when the rotational speed is approximately 25 rpm. The frictional moment of the rotor component is 150g·cm; the maximum synchronizing moment is 900g·cm when the motor has a source voltage of 45V; and the initial rotational speed is 10 rpm for variable-frequency starting. From Fig. 3, the allowance of the motor starting moment is 9, and the allowance of the operating moment is 5; this ensures operational reliability of the motor. In order to solve the problem of wide-range frequency-varying speed-adjustment motor starting, a numerical phase splitting variable frequency power source was developed.

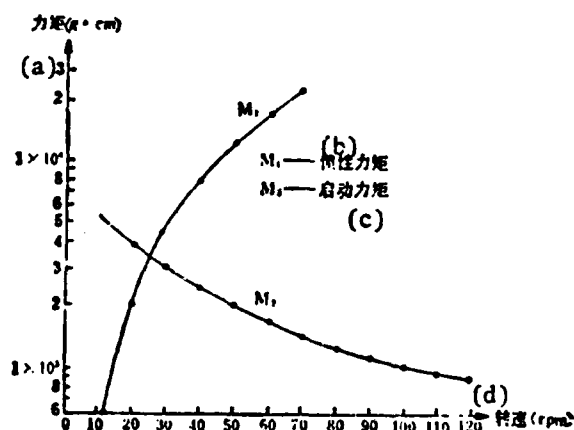


Fig. 3. Starting characteristics of scanning mirror component.
Key: (a) Moment; (b) Inertia moment; (c) Starting moment; (d) Rotational speed.

4. Lubrication of rotating components in very high vacuum

Above a 700-km orbit, the degree of vacuum of a satellite's space environment is higher than 10^{-8} Torr. For an optical scanning system, there

are problems of lubricating rotational components and of operational life span in conditions of very high vacuum.

There are two generally used space lubrication methods: solid lubrication and oil-gas lubrication. According to availability abroad and existing domestic conditions, we selected an oil-gas lubricating structure with oil bearing retainer frame and labyrinth sealing of the protruding part of the rotational shaft. This plan was tested for long service life under high-vacuum ground conditions.

Analyzing the ring-shaped pipeline in Fig. 4, r_1 represents the inner diameter of the rotational shaft; r_2 represents the outer diameter of the shaft hole. When the average free stroke λ of gas molecules is considerably greater than the shaft radius, the gas conduction F of the ring-shaped pipeline is:

$$F = 30.48 \sqrt{\frac{T}{M}} \frac{(r_2^2 - r_1^2)(r_2 - r_1)}{l}, [l, s] \quad (5)$$

In the equation, T is the absolute temperature; M is the gram molecular weight of the gas; and l is the length of pipeline.

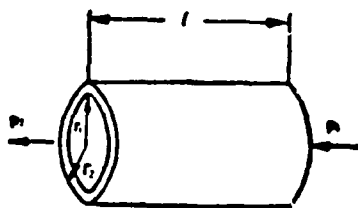


Fig. 4. Ring-shaped pipeline.

The gas flow U (in the ring-shaped pipeline) is:

$$U = (P_1 - P_2) F, [\text{Torr} \cdot l, s], \quad (6)$$

In the equation, $(P_1 - P_2)$ is the pressure difference between two sides of the ring-shaped pipeline.

From Eq. (6), the gas outflow from the ring-shaped pipeline is related to pressure difference and gas conduction. In outer space, $P_2 = 0$, therefore the pressure difference between two sides of the ring-shaped pipeline is primarily determined by the gas pressure within the rotational device. Based on the analysis mentioned above, only by selecting a lubricating oil with low saturated vapor pressure, and by controlling the length of the gap of the protruding portion of the rotational shaft, and by storing sufficient lubricating oil in the motor oil storage device and the bearing retainer frame can a saturated vapor pressure of the lubricating oil be maintained for a long time in the motor to achieve the purpose of bearing lubrication.

We selected #114 silicone oil as lubricant with a gram molecular weight of 8047, 1×10^{-7} Torr as the saturated vapor pressure at 50°C , and dimensions of labyrinth clearance: $r_2 = 1.1$ cm, $r_1 = 1.095$ cm, and $l = 1$ cm. As calculated from Eq. (6), the total amount of lubricating oil (escaping into outer space from two openings of labyrinth clearance in a year) is 1 mg. If 100 mg of lubricating oil is stored in the scanner, two years' continuous operation of the scanner in orbit can be ensured.

In order to certify the above-mentioned scheme, we conducted a simulation test by placing the scanning components into a KM-0.5 container and operated a Model 2TL-500 sputtering titanium pump up to 3×10^{-7} Torr. The scanner operated continuously for half a year at 120 rpm; no appreciable variation of bearing friction moment was discovered.

5. Radiation calibration in flight

In order to deduce radiation intensity and temperature of a target, from the output signal of an infrared scanner, it is required to conduct radiation calibration of the scanner.

With a cold space background (3K) in outer space, the radiation emissivity is only $1/10^{125}$ of a normal-temperature target; this can be the zero radiation

basic reference standard of the scanner. The amplitude of the output signal of an infrared TdCdHg detector is of microvolt magnitude. In order to avoid dc drift in the amplification process of weak signals, ac coupling is adopted for the infrared prime amplifier. Since the coupling capacitor separates the dc component into signals, the output of the prime amplifier only reveals the variation in radiation received. In order to measure the absolute intensity, when a scanner observes cold space, a logic control circuit produces a dc restoration pulse to operate a dc restoration capacitor C of a restoration amplifier to rapidly discharge against the ground via a conduction diode D, thus establishing a zero signal power level (see Fig. 5) corresponding to zero radiation in space. The diode is shut off after the dc restoration pulses pass. If $RC > (1/\omega_L)$ (ω_L is the lower frequency limit of the channel amplifier), the capacitor C exerts a clamp function of zero power level. Later, the amplitude V_1 of the output signal is proportional to the absolute radiation intensity of the target received by the scanner.

$$V_1 = \frac{1}{\pi} K \Omega A \int_{\lambda_1}^{\lambda_2} \mathcal{R}(\lambda) \tau_o(\lambda) P(\lambda, T_{\text{target}}) d\lambda, \quad (7)$$

$$P(\lambda, T_{\text{target}}) = \frac{C_1}{\lambda^5 (e^{C_2/\lambda T} - 1)}, \quad (*)$$

Key: *) target.

In the equation, T_{target} is the target temperature; $C_1 = 3.74 \times 10^{-2} \text{ W} \cdot \text{cm}^2$; $C_2 = 1.438 \text{ cm} \cdot \text{K}$; $\tau_o(\lambda)$ is the optical efficiency; $R(\lambda)$ is the response rate of the detector; A is the radiation receiving area of the optical system; Ω is the instantaneous visual field; and K is the electronic amplification time.

In order to measure the radiation absolute intensity of a target corresponding to signal V , a reference black body (for example, the shell of an instrument can be made into a reference black body) is introduced in an instrument. If the output signal is V_2 when the scanner observes the reference black body, then:

$$V_2 = \frac{1}{\pi} K \Omega A \int_{\lambda_1}^{\lambda_2} \mathcal{R}(\lambda) \tau_o(\lambda) P(\lambda, T_{\text{ref}}) d\lambda, \quad (8)$$

Key: *) reference.

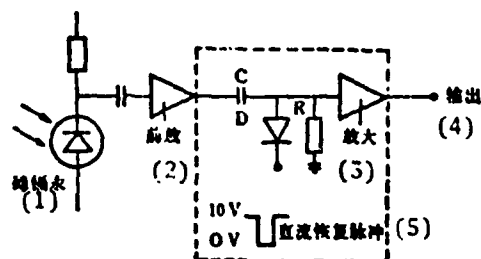


Fig. 5. Diagram showing principle of dc restoration amplifier.

Key: (1) TeCdHg; (2) Prime amplifier; (3) Amplification; (4) Output; (5) dc restoration pulse.

In the equation, $T_{\text{reference}}$ is the temperature of a reference black body, then:

$$\frac{V_1}{V_2} = \frac{\int_{\lambda_1}^{\lambda_2} \mathcal{R}(\lambda) \tau_o(\lambda) P(\lambda, T_{\text{ref}}^{(1)}) d\lambda}{\int_{\lambda_1}^{\lambda_2} \mathcal{R}(\lambda) \tau_o(\lambda) P(\lambda, T_{\text{ref}}^{(2)}) d\lambda} \quad (9)$$

Key: (1) target; (2) reference.

In the above equation, the ratio of V_1 and V_2 can be measured at the ground surface. $T_{\text{reference}}$ can be obtained by temperature remote sensing of the reference black body. Hence, the equivalent black-body temperature of the target can be revealed by using Eq. (9).

6. Radiation calibration of ground surface

The response rate $R(\lambda)$ of a detector can be kept unchanged by accurately controlling cold-block temperature of the radiation cooler. However, the optical efficiency $\tau_o(\lambda)$ of the scanner will vary with the instrument

temperature (primarily determined by the color division lens and light filtering lens). Limited by the structure and weight of the satellite-borne instrument, the blackness of the reference black body cannot be made very high. Hence, radiation calibration should be done on the ground before launching of the scanner in order to obtain a set of the following calibration curve for users' reference (see Fig. 6).

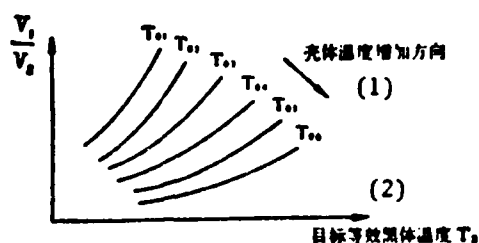


Fig. 6. Radiation calibration curves of radiometer.

Key: (1) Direction of temperature increase of the shell; (2) Equivalent black body temperature T_2 of the target.

For a scanner including a radiation cooler, the radiation calibration of the infrared channel should be conducted in a vacuum system of simulated cold background. The temperature of the cold background should be below 33K; in that case, the effect on the cooling capacity of the second-stage cold block is less than 1 percent. During the experiment, the radiation cooler is aimed at the cold shield, and a liquid nitrogen heat sink (generally, the temperature is 90K; the radiation intensity within $10.5\sim 12.5\ \mu\text{m}$ is only 1/10,000 of the 270K black body target) of a vacuum container is used as the reference datum of zero radiation during dc restoration of signals.

During calibration, a honeycomb surface source can be used as the standard black body; dimensions of the surface source should be able to fill the light passage diameter and instantaneous visual field of the scanner. Based on

manuscript reports, if for each honeycomb element of 6 mm wide, 25 mm long, and 0.05 mm in wall thickness, coating black paint on the surface with thermal radiation efficiency $\epsilon=0.95$, then the equivalent thermal radiation efficiency $\epsilon_1=0.996$. This corresponds to a temperature difference of 0.23K (at 270K) with an ideal black body.

In order to further increase the thermal radiation efficiency of the surface source black body, the honeycomb surface source board can be made into a cavity, as shown in Fig. 7. The ratio between diameter and length of the opening should be 1:2. According to Gouffe's formula, we estimate the equivalent thermal radiation efficiency ϵ_2 of the cavity body as:

$$\epsilon_2 = \frac{\epsilon_1(1+m)}{\epsilon_1(1-A/S) + A/S}, \quad (10)$$

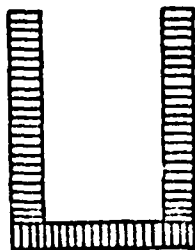


Fig. 7. Cavity-shaped honeycomb surface source black body.

In the equation, at the cavity wall the equivalent thermal radiation efficiency (of the cavity wall) $\epsilon_1=0.996$; the ratio (between opening area and the cavity surface area) $A/S=1/12$,

$$m = (1-\epsilon_1)(A/S - A/S_0) = 0.001\left(\frac{1}{12} - \frac{1}{4\pi}\right) = 6 \times 10^{-5},$$

S_0 is the surface area of a sphere with its diameter equal to the cavity depth. Then we can calculate: $\epsilon_2=0.99976$. This reveals that the error of equivalent black body temperature (at 270K) is less than 0.01K due to thermal radiation efficiency. Then the radiation calibration accuracy of the scanner is determined by the temperature error of the cavity-shaped surface source black body, and the signal-to-noise ratio and signal processing method of the output signals of the scanner.

LITERATURE

- [1] Haviland B. P. and House, C. M., *Handbook of Satellites and Space Vehicles*, New York: D. Nostrand Comp. 1965.
- [2] Guthrie A., *Vacuum Technology*, New York: Wiley, 1963.
- [3] Baker M. L. and MacGarrison M. W., *An Introduction to Astrodynamics*, Academic Press, 1969.
- [4] *Advanced Very High Resolution Radiometer, Final Engineering Report*, NASA CB-156682, 1978.
- [5] *The TIBOS N/NOAA A-G Satellite Series*, NESS-95, 1978.
- [6] *ITOS Meteorological Satellite System, Final Engineering Report*, NASA CB-180163, 1978.

7. Hartson, R. D., Junior, *Principle of Infrared System*, National Defense Industry Publishing Service, 1975.

8. Qin Zifei, Weite Dianji (Micromotor for Special Usages), (1979), Issue No. 1.

INFRARED REMOTE SENSING OF OVER-LAND ATMOSPHERIC TEMPERATURE PROFILES FROM SATELLITE

Zhao Gaoxiang

Institute of Atmospheric Physics, Chinese Academy of Sciences

Received 8 July 1981

The effects of the surface parameters, ϵ and T_s , on atmospheric temperature retrievals, and the possibility of recovering simultaneously both ϵ , T_s , and atmospheric temperature profiles are studied. The results of numerical simulations show that, when one of the two surface parameters is known, atmospheric temperature profiles can be derived and at the same time the other surface parameter can be determined accurately; and even if both ϵ and T_s are unknown, atmospheric temperature profiles and the two parameters can still be recovered with good accuracies.

I. FOREWORD

Satellite remote sensing can provide the atmospheric temperature contour lines from the ground surface to the top of the stratosphere over the entire globe (including continents and oceans). Since the ground characteristics are more complicated than those of oceans, the thermal radiation efficiency

and ground temperature are not easy to predict; correspondingly, retrievals of the atmospheric temperature over land are difficult.

For a group of temperature measuring channels of a satellite, the measured upward radiation intensity of the i -th channel can be expressed as:

$$R_i = [\epsilon_i B_i(T_s) + (1 - \epsilon_i) \hat{R}_{i\downarrow}] \tau_i(P_s) + \int_{P_s}^0 B_i(T) d\tau_i(P), \quad (1)$$

($i = 1, 2, \dots, M$)

Here, M represents the number of channels; ϵ is the thermal radiation efficiency at the ground surface; B is the Planck function; $\hat{R}_{i\downarrow}$ is the effective downward atmospheric radiation intensity; $\tau(P)$ is the transmissibility from the atmospheric pressure P to the top of the atmosphere; the subscript i represents the amount of the i -th channel; T is the atmospheric temperature at the atmospheric pressure P ; and T_s and P_s represent, respectively, the temperature and atmospheric pressure at the ground surface.

From the above transmission equation (1), to solve for the atmospheric temperature contour lines, it is assumed that the efficiency of the ground thermal radiation is known (generally, the ground surface is considered as a black body; that is, $\epsilon=1$), assuming that P_s is the average atmospheric pressure at the sea surface and T_s is measured from the channel of the spectral window; all these parameters are known^[1-3]. Or T_s is considered unknown and is derived together with the atmospheric temperature^[4,5]. For the sea surface, the thermal radiation efficiency is close to 1, since the thermal radiation efficiency can be considered as a known constant at least for a selected group of remote sensing channels. Hence, the above processing is appropriate. There are different conditions over the land; although the atmospheric pressure P_s at the ground surface can be determined based on the topographic altitude of various sites, or directly measured^[6] by laser radar from a satellite, yet the thermal radiation efficiency varies obviously with different characteristics of the ground surface, and numerically the value of efficiency may be considerably different from 1. Moreover, the value of thermal radiation efficiency

is different for different wavelength values; obviously, the value is not a constant: Since the thermal radiation efficiency at the ground surface is unable to be accurately determined, the value also affects the ground surface temperature^[11~15] measured by use of channels at the spectral window; thus, the derived T_s may have errors. Hence, the retrievals of the atmospheric temperature over land are more difficult than for the sea surface. It is more so for the non-statistical retrieval method.

At present, the N series TIROS [television and infrared observation satellite] satellites of the United States apply the regression method of zonal statistics for temperature retrievals. In this method, the entire globe is divided into five latitude zones: one zone from 30°S to 30°N, and two zones each from the pole to 60°, and from 60° to 30°. Then the respective regression coefficients can be derived. These regression coefficients can be continuously corrected^[16] by using consistent data values from radio-sondages and satellites. On the other hand, researchers are studying ways of using other than the conventional data; the accuracies of these kinds of retrieval methods are comparable to that using the conventional data.

Authors of the manuscript [17] studied the retrieval method described in manuscript [4], considering the non-black-body ground surface as a black body, and studying the retrieval effects of temperature and atmospheric pressure at the ground surface. In numerical experiments, the given values of the thermal radiation efficiency at the ground surface are 0.85 and 0.95 at the 4.3 μm band, and 0.95 and 0.98 at the 15 μm band. As revealed by results, the errors cannot be neglected.

The paper studies the effects of ϵ and T_s on temperature retrievals, and investigates the possibility of simultaneously deriving ϵ and T_s on one hand, and the atmospheric temperature on the other.

II. MATHEMATICAL PROCESSING

The 15 μm CO_2 band is selected as the temperature measuring channel; then on the right side of equation (1), the ground surface reflection term of

space radiation is much smaller than the ground-surface emission term. Therefore, no appreciable errors will be introduced by using appropriate modes for approximation. As derived from manuscript [17], the effective downward atmospheric radiation intensity $\hat{R}_{i\downarrow}$ can be expressed as

$$\hat{R}_{i\downarrow} = F_i B_i(T_s)(1 - \tau_i(P_s)), \quad (2)$$

In the equation, the factor F_i can be considered as a constant related to the channels; the value of F_i varies very little in different temperature layers of the atmosphere. Therefore, a line-by-line calculation method can be used in advance to derive a group of constants $[F_i]$ corresponding to a group of remote-sensing channels. Thus, equation (1) can be rewritten as:

$$R_i = \{\epsilon_i + F_i(1 - \epsilon_i)[1 - \tau_i(P_s)]\} B_i(T_s) \tau_i(P_s) + \int_{\tau_i(P_s)}^1 B_i(T) d\tau_i(P), \quad (3)$$

It is assumed that the atmospheric pressure P_s at the ground surface is known; in the wave band for a selected group of channels, the ground surface can be considered a gray body (i.e., $\epsilon_i = \epsilon$, $i=1, 2, \dots, M$); then the following equation can be derived from Eq. (3):

$$R_i = R_i^{(0)} + \Delta R_i^{(0)}, \quad (4)$$

In the equation,

$$R_i^{(0)} = [\epsilon^{(0)} + F_i(1 - \epsilon^{(0)})(1 - \tau_i^{(0)})] B_i(T_s^{(0)}) \tau_i^{(0)} + \int_{\tau_i^{(0)}}^1 B_i(T^{(0)}) d\tau_i^{(0)}(P), \quad (5)$$

$$\begin{aligned} \Delta R_i^{(0)} = R_i - R_i^{(0)} = & [1 - F_i(1 - \tau_i^{(0)})] B_i(T_s^{(0)}) \tau_i^{(0)} \Delta \epsilon^{(0)} \\ & + [\epsilon^{(0)} + F_i(1 - \epsilon^{(0)})(1 - \tau_i^{(0)})] \tau_i^{(0)} \left. \frac{\partial B_i(T_s)}{\partial T_s} \right|_{T_s^{(0)}} \Delta T_s^{(0)} \\ & + \int_{\tau_i^{(0)}}^1 \left. \frac{\partial B_i(T)}{\partial T} \right|_{T^{(0)}} \Delta T^{(0)} d\tau_i^{(0)}(P), \end{aligned} \quad (6)$$

In equations (5) and (6), $\tau_{iS} = \tau_i(P_s)$ (as in the following). The entire atmospheric layer above the ground surface can be divided into N thin layers; by using the numerical integration formula, the equation (6) can be expressed as:

$$\Delta R_i^{(0)} = R_i - R_i^{(0)} = \sum_{j=1}^{N+1} A_{ij}^{(0)} \Delta X_j^{(0)}, \quad (i=1, 2, \dots, M) \quad (7)$$

In the equation,

$$A_{ij}^{(n)} = \frac{\partial B_i(T)}{\partial T} \Big|_{T_j} [\tau_i^{(n)}(P_{i-1}) - \tau_i^{(n)}(P_i)], \quad (j=1, 2, \dots, N)$$

$$A_{i,N+1}^{(n)} = [\epsilon^{(n)} + F_i(1-\epsilon^{(n)})(1-\tau_{iN}^{(n)})] \tau_{iN}^{(n)} \frac{\partial B_i(T_i)}{\partial T_i} \Big|_{T_j}$$

$$A_{i,N+2}^{(n)} = [1 - F_i(1-\tau_{iN}^{(n)})] B_i(T_i^{(n)}) \tau_{iN}^{(n)},$$

$$\begin{cases} \Delta X_j^{(n)} = \Delta T_j^{(n)}, & (j=1, 2, \dots, N), \\ \Delta X_{N+1}^{(n)} = \Delta T_{N+1}^{(n)}, \\ \Delta X_{N+2}^{(n)} = \Delta \epsilon^{(n)}, \end{cases}$$

$P_0 \approx 0$ and $\tau_i(P_0) \approx 1$; T_j is the average temperature of the j -th layer of the atmosphere. By using the method in manuscript [5], equation (7) can have solutions in matrix form:

$$\Delta \mathbf{X}^{(n)} = (\mathbf{A}^{(n)})^* [\mathbf{A}^{(n)} (\mathbf{A}^{(n)})^* + r \mathbf{I}]^{-1} \Delta \mathbf{R}^{(n)}, \quad (8)$$

$$\mathbf{X}^{(n+1)} = \mathbf{X}^{(n)} + \Delta \mathbf{X}^{(n)}, \quad (9)$$

In equation (8), \mathbf{I} is the $M \times M$ -dimension unit matrix; r is a smoothing factor; the superscript represents times of successive substitution; and $\epsilon=0$ is the quantity corresponding to the initial value. The process of successive substitution stops at

$$|\Delta R_i^{(n)}| < \epsilon, \quad (i=1, 2, \dots, M)$$

and ϵ is the observation error.

III. RESULTS AND DISCUSSIONS ON NUMERICAL TESTS

The author and his colleagues used channels (see Table 1) of two groups of triangular response function described in manuscript [5]. The numerical experiments of temperature retrievals were conducted by assuming in the following (different ground-surface conditions) that the atmospheric pressure at the ground surface is 1000 mb; the measurement error is $0.3 \text{ erg} \cdot \text{s}^{-1} \cdot \text{cm}^{-1} \cdot \text{ster}^{-1}$; and the thermal radiation efficiency (at the ground surface) varies between 0.8 and 0.99.

1. ϵ and T_s are known; then $\Delta\epsilon^{(l)}=0$, $\Delta T_s^{(l)}=0$, the coefficient matrix $A^{(l)}$ degenerates into a $M \times N$ -dimension matrix.

2. It is assumed that the ground surface is a black body ($\epsilon^{(l)}=0$), and T_s is an unknown. Then, $\Delta\epsilon^{(l)}=0$; the coefficient matrix $A^{(l)}$ is a matrix of $M \times (N+1)$ -dimension.

3. ϵ is a known quantity but T_s is unknown. Then, $\Delta\epsilon^{(l)}=0$; the coefficient matrix $A^{(l)}$ is a matrix of $M \times (N+1)$ dimensions.

4. ϵ is an unknown quantity but T_s is known by assuming that there are deviations of 0°C , 2°C and 5°C between T_s and the "real" ground-surface temperature. Then, $\Delta T_s^{(l)}=0$; the coefficient matrix $A^{(l)}$ degenerates into a matrix of $M \times (N+1)$ -dimension.

5. Both ϵ and T_s are considered unknown quantities to be determined. Then, the coefficient matrix $A^{(l)}$ is a matrix of $M \times (N+2)$ -dimension.

Table 1. Number of channels and center frequencies of various channels for two groups of temperature measurement channels.

(a) 序号	通道数	(e) 各 通 道 中 心 频 率 (cm^{-1})
(b) 第一组	(d) 7	604, 679.5, 692, 704.5, 717, 732, 747
(c) 第二组	17	668, 672, 677, 682, 687, 692, 697, 700.3, 702, 707, 712, 717, 722, 732, 747, 752, 757

Key: (a) Sequence number; (b) First group; (c) Second group; (d) Number of channels; (e) Center frequencies (cm^{-1}) of various channels.

Table 2 shows the results obtained in numerical experiments in different conditions at the ground surface. The results include the root mean square RMS($^\circ\text{C}$) of the atmospheric temperatures of 37 pressure layers in all from 10 mb to the ground surface; the root mean square deviation ($^\circ\text{C}$) from the ground-surface temperature of 19 layers (of the 37), and the root mean square deviation $\Delta\epsilon$ of the thermal radiation efficiency of the ground surface.

Table 2. Partial results of numerical experiments.

No.	Pressure (b)	(c) Δ															
		Ground surface conditions								Unknown							
		T _g = T _g				T _g = T _g				T _g = T _g				T _g = T _g			
		T _g = T _g	T _g = T _g	T _g = T _g	T _g = T _g	T _g = T _g	T _g = T _g	T _g = T _g	T _g = T _g	T _g = T _g	T _g = T _g	T _g = T _g	T _g = T _g	T _g = T _g	T _g = T _g	T _g = T _g	T _g = T _g
15	18.50	5.56	4.73	5.42	5.52	5.48	1.95	1.92	2.18	1.92	1.94	1.90	1.86	1.95	1.91	1.91	1.90
17	24.98	2.90	2.48	2.78	2.87	2.83	2.35	2.31	2.50	2.34	2.34	2.30	2.25	2.35	2.32	2.31	2.30
19	36.17	2.60	2.41	2.52	2.60	2.57	2.67	2.71	2.72	2.71	2.71	2.70	2.67	2.70	2.71	2.71	2.71
21	50.56	2.22	2.14	2.23	2.24	2.25	1.89	1.93	1.93	1.91	1.92	1.92	1.91	1.91	1.93	1.91	1.92
27	66.64	3.91	3.48	3.90	3.94	3.92	1.95	1.95	1.99	1.99	1.97	1.95	1.97	1.96	1.93	1.96	1.92
29	90.92	4.70	4.24	4.57	4.67	4.63	1.84	1.86	1.92	1.83	1.84	1.81	1.76	1.85	1.85	1.84	1.83
27	117.94	3.98	3.71	3.81	3.91	3.84	1.98	1.96	2.13	1.94	1.99	1.95	1.88	2.00	1.96	2.00	2.00
29	150.26	3.08	2.97	2.92	2.10	2.09	1.92	1.93	2.10	1.93	1.93	1.90	1.87	1.93	1.93	1.93	1.91
31	185.45	3.18	2.81	3.17	3.24	3.22	2.30	2.30	2.39	2.31	2.31	2.28	2.25	2.32	2.30	2.32	2.32
33	233.12	3.08	3.63	3.54	3.54	3.54	2.64	2.61	2.56	2.36	2.64	2.62	2.52	2.37	2.51	2.57	2.56
35	294.89	2.94	3.04	2.94	2.98	2.99	1.32	1.33	1.56	1.33	1.35	1.32	1.29	1.34	1.33	1.35	1.36
37	344.38	2.97	2.88	3.13	3.17	3.17	2.61	2.58	2.73	2.64	2.64	2.60	2.51	2.64	2.59	2.65	2.65
39	412.26	3.22	3.21	3.44	3.39	3.43	2.35	2.26	2.64	2.41	2.44	2.38	2.22	2.40	2.27	2.43	2.43
41	494.20	2.23	2.21	2.20	2.44	2.34	1.90	1.87	1.70	1.68	1.65	1.95	2.18	1.66	1.86	1.84	1.82
43	575.60	2.96	2.65	3.55	3.36	3.58	2.14	2.14	2.14	2.39	2.15	2.54	2.91	2.30	2.14	2.33	2.30
45	673.03	2.64	2.56	3.37	2.93	3.02	2.42	2.33	2.78	2.48	2.45	2.46	2.44	2.44	2.34	2.48	2.46
47	781.34	2.41	2.55	2.33	2.61	2.45	2.20	2.24	3.07	2.18	2.14	2.48	3.05	2.13	2.26	2.10	2.09
49	901.54	3.19	4.41	3.88	4.23	3.97	2.10	2.87	8.39	2.10	1.94	8.73	7.67	2.08	2.74	2.01	1.99
50	946.38	1.76	1.68	2.90	1.99	2.03	1.11	1.56	1.19	1.11	1.04	1.20	1.63	1.04	1.05	1.00	0.98
50*	1000.0	0	4.50	5.47	0.51	0	0	1.13	6.76	0.15	0	2	5	0	1.79	0.17	0
50 RMR %		3.16	2.92	3.21	3.27	3.22	2.05	2.08	2.59	2.08	2.04	2.18	2.65	2.05	2.08	2.05	2.04
Δ		0	0.0776	0.1033	0	0.0082	0	0.0154	0.1033	0	0.0022	0.0282	0.0697	0	0.0237	0	0.0023

Remarks: (1) The column marked with * shows results of 210 numerical experiments; the other columns show the results of 289 numerical experiments. (2) c and T_g are, respectively, the ground-surface thermal radiation efficiency and the ground-surface temperatures; c' and T'_g are, respectively, the assumed known ground-surface thermal radiation efficiency and the ground-surface temperature.
Key: (a) Number of layers; (b) Pressure; (c) Number of channels and ground-surface conditions; (d) Unknown; (e) Ground surface.

From Table 2, results obtained by use of 17 channels are obviously better than those obtained for 7 channels; this is consistent with results^[5] of retrievals of the atmospheric temperature over the sea surface. Let us investigate, in the following, the results obtained by use of 17 channels of temperature measurement. Under the condition that both ground-surface parameters, ϵ and T_s , are accurately known, the retrieval results of the atmospheric temperature are the best. However, by only having one of two (ϵ and T_s) as a known quantity, we also obtained the same good results; moreover, at the same time, another ground-surface parameter can be accurately obtained. When T_s is known, the obtained (root mean square) deviation of the thermal radiation efficiency is 0.0022; when ϵ is known, the obtained (root mean square) deviation of T_s is 0.15°C. However, when errors develop in one ground-surface parameter, other errors also exist in the retrieval of the other ground-surface parameter (and at the same time, the error is increased in retrieval of the atmospheric temperature). This effect exists, primarily, in several layers close to the ground surface.

Also from Table 2, when T_s and ϵ are known, the retrieval accuracy of the atmospheric temperature is also comparable to the condition that both T_s and ϵ are known. In addition, values of T_s and ϵ can be simultaneously and accurately obtained; the deviations of the root mean square of the two are, respectively, 1.13°C and 0.155. While one mode of atmosphere and two radiosonde temperature contour lines are considered the "real" situation, Figure 1 shows the comparison of retrieval results assuming that both T_s and ϵ are known, and both T_s and ϵ are unknown in two different conditions at the ground surface. Of the retrieval results under the two conditions, there are only small differences at layers close to the ground surface; these two results are almost entirely identical for higher layers.

While accurately knowing the contribution of the ground surface to the emergent radiation, there is no effect on retrieval of the atmospheric temperature by the ground-surface parameters. The situation is similar when both the ground-surface parameters ϵ and T_s are known. Under other situations,

there is some difference from the above-mentioned situation for the retrieval results of the atmospheric temperature; this difference is primarily due to errors in ground-surface parameters. However, relatively speaking, errors in ground-surface parameters do not have an appreciable effect on differences in the atmospheric temperature. From Table 2, the effect of errors (between ϵ and T_s) is close to a proportional relationship. In Equation (5), the main contribution to the ground surface is from the ground-surface emission term; this also means that the functions of ϵ and T_s are mutually compensated to a very considerable extent. This indicates that there is a closer relationship between two ground-surface parameters than between two parameters and the atmospheric temperature. Just because both inherent relation and relative independence exist between the ground-surface parameters and the atmospheric temperatures, we can possibly determine ground-surface parameters with satisfactory accuracy while deriving the atmospheric temperatures.

We know that following the correction of the atmospheric effect, when one of the two (ground-surface parameters, ϵ and T_s , of a channel of the spectral window) is known, the other parameter can be determined. Both ϵ and T_s can be simultaneously determined for two channels of the spectral window with the same thermal radiation efficiency. Under situations of this type, errors of the obtained ground-surface parameters are determined by whether or not corrections of the atmospheric effect are accurate if other errors are not considered. Among temperature-measurement channels we used, those channels having the ground-surface transmissibility not equal to zero also include signals of ground-surface parameters. However, these channels are within the absorption zone, with considerable effect played by the atmosphere, so it is even more difficult in correction. Comparing the obtained temperature contour lines with the real contour lines in temperature retrievals, oftentimes when positive deviations exist in some layers, negative deviations exist in the adjacent layers. Therefore, the contribution of the entire atmosphere (the last term on the right side of equation (3)) is still possibly close to the real value. For the ground-surface transmissibility, there is no major effect on different temperature layers of the atmosphere. Thus, equations of ground-surface parameters can be derived from equation (3); it is possible to determine ϵ and T_s like that in the spectral window zone. The number of

signals of ground-surface parameters contained by these channels is smaller than those in the spectral window zone; errors with corrections of the atmospheric effect may be relatively great. Furthermore, by considering the existence of the observation errors, the ground-surface parameters cannot be determined as well as that for the situation of the spectral window zone with the same number of channels. For compensation of this point, it is required to adopt more channels including signals of the ground surface and the atmosphere; this point is illustrated by the fact that better results can be obtained by using 17 channels than 7 channels.

The last four columns in Table 2 show results in the retrieval process as the group of coefficients $[F_i^*]$ are smaller by 10 percent (represented by F_{i0}^* in the table) than the real values in the retrieval process. We can see that there are very small differences from results obtained by use of the correct coefficient $[F_i^*]$ under the corresponding conditions. Only when both ϵ and T_s are unknown are there somewhat greater errors (respectively at 1.79°C and 0.0237) for the obtained retrieval ground-surface temperatures and thermal radiation efficiencies; however, the effect of the retrieval atmospheric temperature is not great even in this situation. This illustrates that the radiation term reflected to space from the ground surface is small compared with the emission term. Therefore, some errors will not cause a serious effect on retrieval in the calculation coefficient $[F_i^*]$. This point is advantageous in actual application.

In the situation when the atmospheric pressure at the ground surface is some other value, similar results can also be obtained. Figure 2 shows results when the ground-surface atmospheric pressure $P_s = 700$ mb. We can see that quite good results can still be obtained when both the ground-surface parameters, ϵ and T_s , are unknown. Figure 2 (a) shows an example; Figure 2 (b) shows the root mean square deviations of all layers below 10 mb as obtained in 289 numerical experiments.

Since the situation of the ground surface varies with locations and seasons, the thermal radiation efficiency at the ground surface varies with

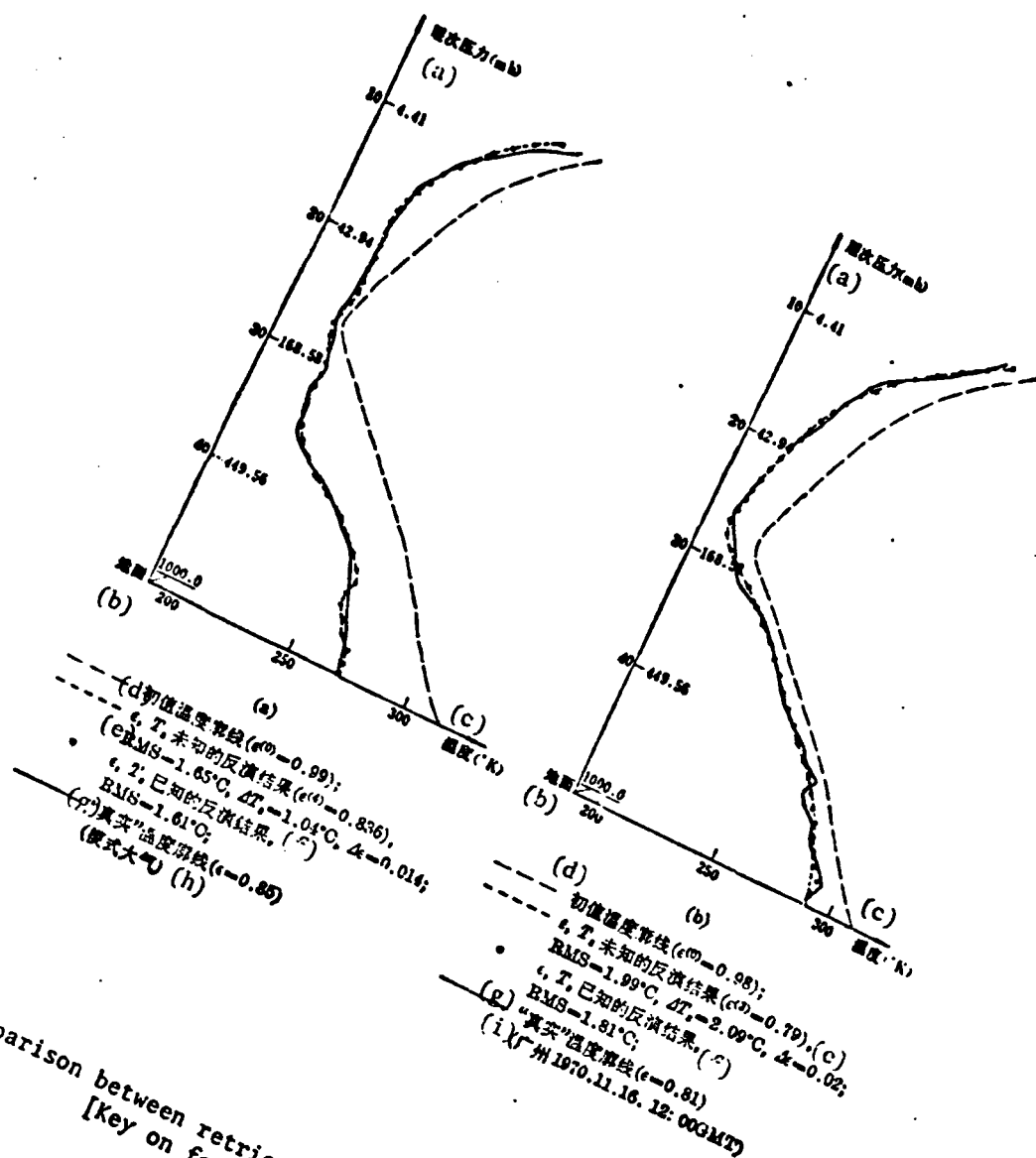


Fig. 1. Comparison between retrieval results and the "real" temperature contour lines.
[Key on following page]

[Fig. 1 continued]

Key: (a) Pressure at particular layer; (b) Ground surface; (c) Temperature; (d) Initial value of temperature contour line; (e) Retrieval results when both ϵ and T_s are unknown; (f) Retrieval results when both ϵ and T_s are known; (g) "Real" temperature contour line; (h) Mode of atmosphere; (i) Guangzhou.

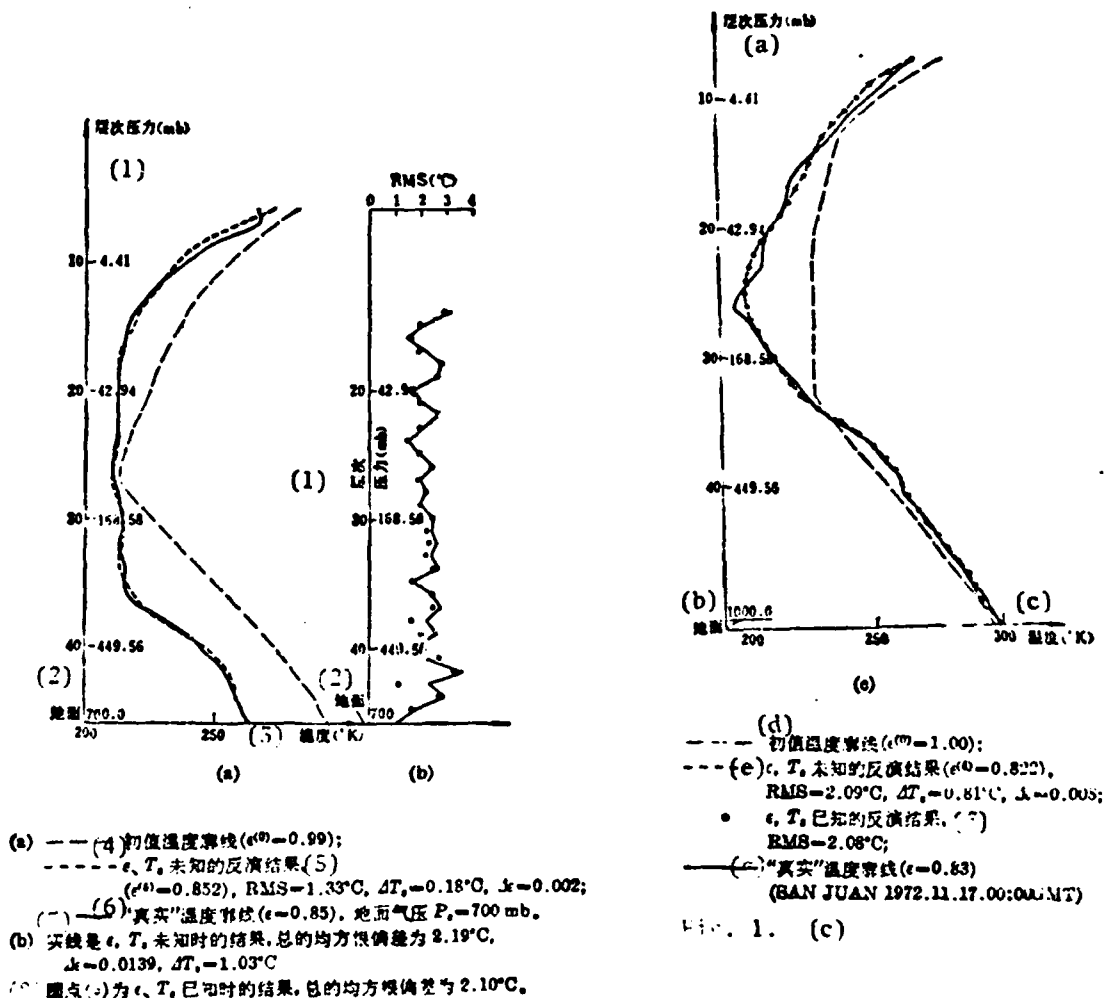


Fig. 2. Temperature retrieval results when the ground-surface atmospheric pressure $P_s=700$ mb.

Key: (1) Pressure (mb) at the particular layer; (2) Ground surface; (3) Temperature; (4) Initial values of temperature contour lines; (5) Retrieval results when both ϵ and T_s are unknown; (6) "Real" temperature contour line ($\epsilon=0.85$) with ground-surface atmospheric pressure $P_s=700$ mb; (7) Solid line shows results when

[Key (of Fig. 2) continued]

both ϵ and T_s are unknown; the root mean square deviation of all layers is 2.19°C ; (8) Circles (*) indicate results when both ϵ and T_s are known; the root mean square deviation of all layers is 2.10°C .

wavelengths. Therefore, it is a very difficult problem to accurately determine (in advance) the ground-surface parameters, ϵ and T_s , by some means while seeking retrievals of the atmospheric temperature. However, from the above-mentioned results, the ground surface can be considered as a gray body in a spectral region of the selected group of temperature-measurement channels (actually, within the range of several channels when the ground-surface transmissibility is not equal to zero). Thus, no other means is required to know, in advance, the ground-surface parameters; the atmospheric temperatures and the ground-surface parameters can be simultaneously obtained directly from these temperature-measurement channels. This is very significant.

The author expresses his gratitude to Comrade Zhou Xiuji for his revision and for providing valuable counsel.

LITERATURE

1. Zeng Qingcun, Daqi Hongwai Yaoce Yuanli [The Principle of Atmospheric Infrared Remote Sensing], Science Publishing House, 1974.
2. Yuan Zhongguang and Zeng Qingcun, Qixiang Weixing Di Hongwai Yaoce Ji Fanyan (Yi) [Infrared Remote Sensing and Retrievals of Meteorological Satellites (I)], Science Publishing House, 1977, 19.
3. Wark, D. Q., and Fleming, H. E., Mon. Weather Rev., 94 (1966), 6, 351.
4. Chahine, M. T., J. Opt. Soc. Am., 58 (1968), 12, 1634.
5. Zhao Gaoxiang, Kexue Tongbao [Science Bulletin], 25 (1980), 23, 1079.

[6] Singer B. F., *Appl. Opt.*, 7 (1968), 6, 1125

[7] Buettner K. J. and Fenz, C. D., *J. Geophys. Res.*, 70 (1965), 6, 1329.

[8] Vincent R. K. et al., *Remote Sens. Environ.*, 4 (1975), 3, 199

[9] Griggs M., *J. Geophys. Res.*, 73 (1968), 24, 7345

- [10] Hovis W. A. Jr. et al., *Appl. Opt.*, **7** (1968), 6, 1137.
- [11] Weiss M., *Appl. Opt.*, **10** (1971), 6, 1280.
- [12] Lorenz D., *Appl. Opt.*, **7** (1968), 9, 1705.
- [13] Sutherland R. A. et al., *J. Appl. Meteorol.*, **18** (1979), 6, 1163.
- [14] Hovis W. A. Jr., *Appl. Opt.*, **5** (1966), 6, 815.
- [15] Shaw J. H., *J. Atmos. Sci.*, **27** (1970), 6, 959.
- [16] Phillips N. et al., *Bull. Amer. Meteorol. Soc.*, **60** (1979), 10, 1183.
- [17] Kornfeld and J. Susskind, *J. Mon. Weather Rev.*, **105** (1977), 12, 1655.

A METHOD OF DETERMINING THE BRIGHTNESS TEMPERATURE IN A SHORT WAVE INFRARED
ATMOSPHERIC SPECTRAL WINDOW FROM SATELLITE MEASUREMENT

Wang Qinmo

Satellite Meteorological Center, Central Meteorological Bureau

Received on 18 July 1981; the revised paper was received on 14 February 1982.

Presented in this paper is a formula of calculating brightness temperature in short-wave IR atmospheric window from instantaneous radiance measurements of two channels in $3.7\sim 4.0\mu\text{m}$ spectral band by polynomial fit technique. Its accuracy is within $\pm 0.4\text{K}$. The approach for determining corrections of reflected solar radiance on measurements in $4.8\mu\text{m}$ CO_2 absorption band is briefly described.

I. FOREWORD

There are two channels (HIRS/2-18 and HIRS/2-19) of a short wave infrared (IR) atmospheric spectral window in the improved model of high discriminability IR detector (HIRS/2) in the TIROS-N meteorological satellites of the United States; the number of center waves is, respectively, 2511.95 cm^{-1} and 2671.18 cm^{-1} , marked as W_1 and W_2 . By using the simultaneous radiance measurements of

these two channels, the reflectivity of the earth's surface can be calculated, and the effect on the temperature detection channel of the $4.3 \mu\text{m}$ CO_2 absorption band on the solar radiation reflected from the earth's surface can be estimated.

II. CALCULATION METHODS

The response to water vapor by the short wave IR atmospheric spectral window is considerably weaker than that of the long wave IR atmospheric spectral window ($11.0 \mu\text{m}$). Therefore, not as in the case of the long wave, water vapor absorption is a factor that should be considered first. However, the extra-terrestrial radiation reflected from the earth's surface should be considered; the reflective component of the downward radiation to the atmosphere (in the reflected radiation) is less than 1 percent of the radiation at the earth's surface; therefore, the reflective component can be neglected. However, the reflected solar radiation is about 1/7; this is the factor having a major effect on short wave IR remote sensing during daytime^[1].

For the short wave IR atmospheric spectral window, the radiation transmission equation can be simplified in [2] under cloudless atmospheric conditions:

$$R(W) = \epsilon_s B(W, T_s) + \gamma_s I_s(W) \mu_0 \quad (1)$$

In the equation, $R(W)$ is the measured radiation intensity when the intermediate and short wave IR atmospheric spectral window channel of the IR detector (the number of center waves is indicated by W) aims at the globe. The first term on the right side of equation (1) represents the contribution to $R(W)$ by solar radiation reflected from the earth's surface. γ_s and ϵ_s are, respectively, the reflectivity and thermal radiation efficiency of the earth's surface; μ_0 is the cosine of the zenith angle θ_0 of the sun; when θ_0 is greater than 90° , $\mu_0 = 0$. $B(\nu, T)$ is the spectral radiation intensity (also called the Planck function) at wave number ν of a black body with temperature T .

$$B(\nu, T) = \frac{c_1 \nu^3}{\exp(c_2 \nu / T) - 1}$$

In the equation, c_1 and c_2 represent, respectively, the first and second radiation constants; $c_1 = 2hc^2$ and $c_2 = hc/k$.

I_0 is the solar radiation intensity arriving at the earth's surface; the approximate expression of I_0 is:

$$I_0(W) = B(W, T_{\text{sun}}) \frac{\Omega_{\text{sun}}}{\pi}, \quad (2a)$$

In the equation, T_{sun} is the brightness temperature of the sun, generally at 5800~6000K; Ω_{sun} is the included solid angle of the earth by the sun and is a constant, approximately 7×10^{-5} sr. Here we assume that in magnitude the direct solar radiation is equivalent to radiation intensity of a black body with temperature T_{sun} .

If the microabsorption effect of the gaseous components of the atmosphere on the solar radiation in the short wave IR spectral window is included, equation (2a) is revised as:

$$I_0(W) = B(W, T_{\text{sun}}) \frac{\Omega_{\text{sun}}}{\pi} \tau^{(\cos \theta_0 + \cos \theta)}(W). \quad (2b)$$

In the equation, $\tau(W)$ is the transmissibility at the upward perpendicular direction of the local site; θ_0 is the zenith angle of the sun; and θ is the zenith angle of the satellite. In these expressions, the form of equation (1) remains unchanged.

By using Smith's assumption^[3] that γ_s and ϵ_s are not related to the approximate value of the wavelength in a narrow short wave IR spectral region from 3.7 μm to 4.2 μm , we obtain equation (3) from equations (1) and (2):

$$\frac{R(W_2) - \epsilon_s B(W_2, T_s)}{R(W_1) - \epsilon_s B(W_1, T_s)} = \frac{B(W_2, T_{\text{sun}})}{B(W_1, T_{\text{sun}})}. \quad (3)$$

For HIRS/2-18 and HIRS/2-19, if $T_{\text{sun}} = 5800\text{K}$, the right side of equation (3) becomes:

$$\frac{B(W_2, T_{\text{sun}})}{B(W_1, T_{\text{sun}})} = K = 1.10635. \quad (4)$$

According to the definition, the brightness temperature T_B satisfies the following equation:

$$\epsilon_0 B(W, T_0) = B(W, T_B). \quad (5)$$

Equation (3) can be rewritten as:

$$B(W_2, T_B) - K B(W_1, T_B) = R(W_2) - K R(W_1). \quad (6)$$

Equation (6) is a transcendental equation related to T_B . We used the polynomial fit method to establish the apparent relationship between $R(W_2)$ on one hand, and T_B and the radiation measurement value $R(W_1)$ on the other. Let

$$f = R(W_2) - K R(W_1), \quad (7)$$

We take the cubic polynomial; i.e.,

$$T_B = \sum_{i=0}^3 a_i [\ln(-f)]^i, \quad (8)$$

From equations (6) and (7), we can calculate the coefficient a_i first. By selecting the temperature range from 200K to 340K (corresponding to two extreme temperatures of the earth), the least squares method is used (on two short wave IR atmospheric spectral window channels of TIROS-N) to establish a linear equation set concerning a_i and to adopt a main element cancellation method for solving the equation set. Table 1 shows the calculation results.

Table 1. Coefficients of the calculated brightness temperatures of HIRS/2 short wave IR spectral window in TIROS-N.

a_0	a_1	a_2	a_3
314.0964	29.1788	2.5256	0.1266

Thus, based on the simultaneous measurement values of channels 18 and 19 of HIRS/2 on the TIROS-B, f is calculated from equation (7); substituting into equation (8), T_B is derived; the error is less than $\pm 0.4K$ (see Table 2).

Table 2. Calculated value (T_B) and simulated value (T) by use of polynomial fit method.

$T(K)$	210	240	260	280	300	320	340
$T_B(K)$	210.08	239.95	259.86	279.97	300.15	320.09	339.68
$T_B - T$	0.08	-0.05	-0.14	-0.03	0.15	0.09	-0.32

It should be pointed out that although the effect of water vapor and other gaseous components is relatively small in the short wave IR atmospheric spectral window, their influence on the measurement values should still be considered, especially in the case when the water vapor content in the low atmospheric layer is relatively great (in this paper, it is assumed that corrective measures are made on absorption of these components before application of equation (8)).

III. CORRECTIONS OF REFLECTIVITY (TERM) OF THE EARTH'S SURFACE AND THE REFLECTED SOLAR RADIATION TERM

After calculating the brightness temperature T_B by using the measurement values of IR atmospheric spectral window channels by use of the satellite-borne IR detector, the reflectivity γ_s is (based on equation (1)):

$$\gamma_s = \frac{R(W) - B(W, T_B)}{I_s(W) \mu_0},$$

If W is substituted by W_1 , we obtain by using equation (2b):

$$\gamma_s = \frac{R(W_1) - B(W_1, T_B)}{B(W_1, T_{\text{sea}})} \left[\frac{\Omega_{\text{sea}}}{\pi} \mu_0 \right]^{-1} \left[\tau^{\text{atm}}_{\lambda_0 + \Delta \lambda} (W) \right]^{-1}. \quad (9)$$

The corrected term $SC(v)$ of the reflected solar radiation of a certain channel (indicated by v , the number of center waves) within the CO_2 absorption zone of $4.3 \mu\text{m}$, actually is the second term on the right side of equation (1).

$$SO(\nu) = \frac{R(W_1) - R(W_1, T_n)}{B(W_1, T_{sun}) / B(\nu, T_{sun})} \left[\frac{\tau(\nu)}{\tau(W_1)} \right]^{n \cos \theta_0 + \sec \theta}, \quad (10)$$

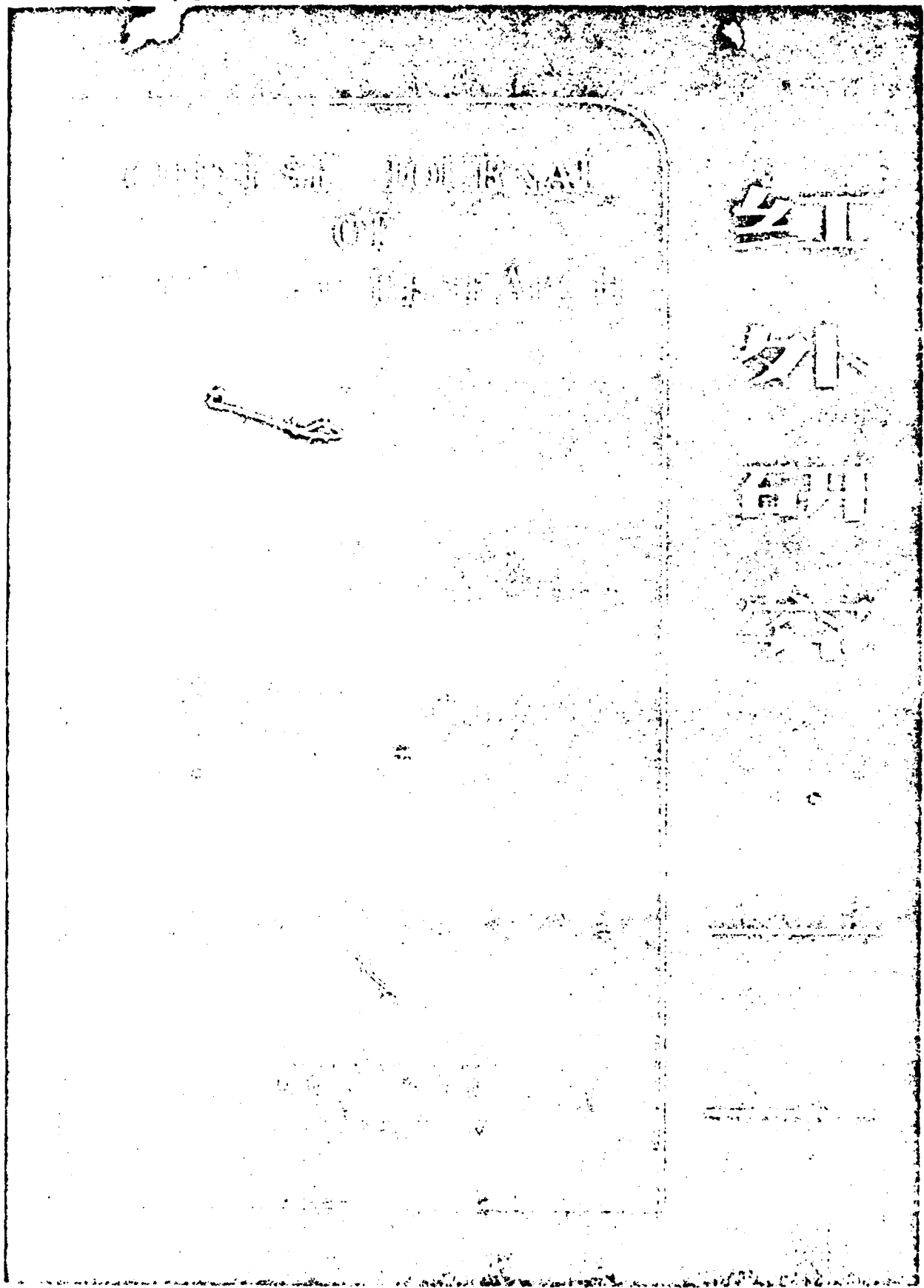
In the equation, the zenith angle θ_0 of the sun can be calculated by using the astronomical formula at the place of the satellite's observation time. There is another parameter, the transmissibility, which should be derived by using an appropriate method in advance.

LITERATURE

1. Zeng Qingcun, Daqi Hongwai Yaoce Yuanli [The Principle of Atmospheric Infrared Remote Sensing], Science Publishing House, 1974.

[2] Smith W. L. et al., *NOAA TM NESS 57*, 1974.

[3] Smith W. L., *WMO/UN Regional Training Seminar on the Interpretation, Analysis and Use of Meteorological Satellite Data*, Tokyo, Japan, 23 Oct. to 2 Nov., 1978.



发展星载红外遥感仪器中的 几个问题及其解决方法*

龚 惠 兴

(中国科学院上海技术物理研究所)

摘要——本文讨论了发展星载红外遥感仪器中需要特殊考虑的几个问题，它们是：扫描周期的确定，扫描器及其在外层空间超高真空环境中的润滑以及仪器的辐射定标等。本文并提出了解决这些问题的方法。

近十年来，随着工作温度为 77 K~105 K、探测率 $D^* > 1 \times 10^{10} \text{ cm} \cdot \text{Hz}^{1/2} / \text{W}$ 、响应时间 $\tau < 1 \mu\text{s}$ 、响应波长 $\lambda_c > 14 \mu\text{m}$ 的碲镉汞红外探测器及长寿命无源辐射制冷器的出现，使光学机械扫描式的红外遥感仪器能在长寿命的业务气象卫星和陆地卫星上，对地球的陆地、大气、海洋作周期性的高分辨观测。由于光机扫描多波段红外遥感仪器具有从可见到长波红外的宽波段观测能力，因此它在空间遥感中占重要地位。

图 1 是一种多波段扫描仪的简化光路结构。它有一块与转轴成 45° 夹角的扫描反射镜，转轴与卫星的飞行方向一致，当扫描镜旋转时，仪器就以固定的光学瞬时视场在垂直于卫星的飞行方向扫描，接收地气系统发射或反射的辐射，借助于卫星绕地球的前进运动，得到大气、陆地、海洋的景像(图 2)。

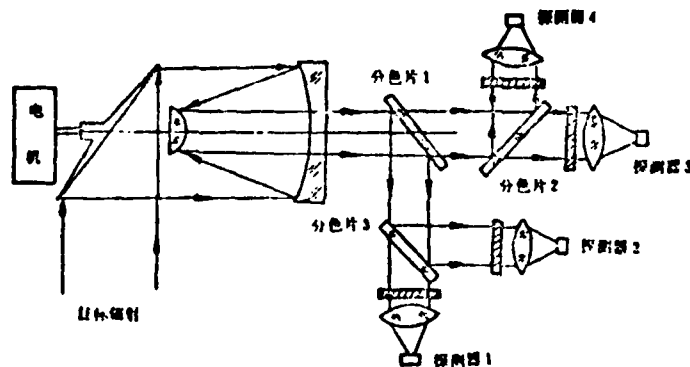


图1 TIROS N AVHRR 四波段红外扫描仪光路示意图

本文1982年1月16日收到。

* 参加本工作的有720组和730组的全体同志。

本文对发展此类遥感仪器中遇到的几个问题及其解决方法作一简要讨论。

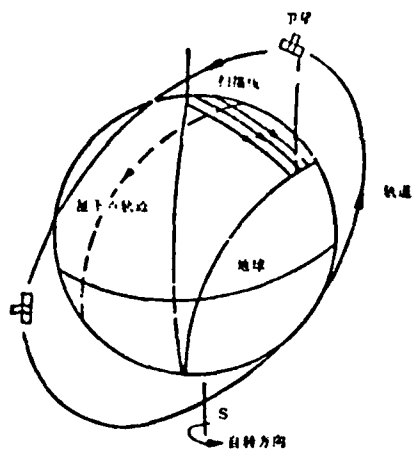


图2 扫描仪拍摄地球景象的原理图

10.5~12.5 μm 的红外大气窗通道的辐射探测,需要使用碲镉汞探测器,它装于两级辐射制冷器的二级冷块上,工作温度为 105 K。为使辐射致冷器与 3 K 冷空间背景有充分的辐射热交换,辐射器开口应一直朝向冷空间。

在对地姿态三轴稳定的卫星中,卫星的偏航和滚动轴以卫星绕地运动相等的角速度绕俯仰轴旋转,因为俯仰轴与轨道平面垂直,所以它在空间相对稳定。因此,在极地及地球同步轨道中,辐射致冷器的开口都取在与俯仰轴一致的背阳方向,为避免阳光对辐射致冷器开口的照射,需要使卫星的轨道平面与阳光交角基本保持不变,即太阳同步轨道。实现太阳同步的方法是控制轨道的发射倾角 i ,当 i 满足

$$i = \cos^{-1} \left[-0.0985(1-e^2)^{1/2} \left(\frac{a}{R} \right)^{1.5} \right] \quad (3)$$

时(其中 e 为轨道偏心率, a 为轨道长半轴),就能使赤道突出部分对卫星运动的摄动,使轨道平面绕地球自转轴的转动,抵消因地球太阳公转带来的轨道平面与阳光交角的变化。在太阳同步轨道时,轨道平面与太阳交角的年变化不超过 $\pm 23.5^\circ$ 。

3. 扫描镜驱动装置

卫星拍摄的地球景象信号,可通过机电同步的地面接收站得到图象。当卫星图象的发送采用窄路模拟信号输出时,因不作有扫描镜转速的同步参考信号,为使地面接收的图象不致产生歪斜和抖动,需要严格控制扫描镜转速的长期及瞬时稳定度。

为简化传动结构和因齿轮带来的磨损和润滑问题,提高寿命和可靠性,可采用 TDB-500 低速永磁式交流同步电机直接传动 45° 扫描镜。TDB-500 是轴向激磁的,按照定子和转子开口槽所造成的气隙磁导变化原理工作的,转子转速 N 为:

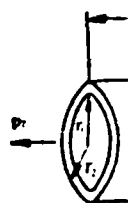
$$N = 60 \times \frac{\text{电源频率}}{\text{转子开口槽数}}, [\text{rpm}] \quad (4)$$

见转子开口槽数为 50,当电源频率为 100 Hz 时,电机转速为 120 rpm。由于是同步电机,转子平均转速取决于电源频率,使用石英振荡分频的电源,能达到 3×10^{-6} 的频率稳定度。电

机按电磁减速
0.8 mrad。

使用同步
1.8°。当转速
组件启动。根
力矩,这大大
电压不变的情
下降。图 3 表
力矩为 150 g·
速在 10 rpm,
可靠性。为解

4. 转动 在七百



分析图
由程入远大

其中, T 是
环形管道中

机按电磁减速原理工作,具有比普通电机高 50 倍的比整步力矩,经实测,扫描镜抖动角小于 0.6 mrad。

使用同步电机的最大缺点是启动比较麻烦,因是减速比为 50 的电机,其最大整步角为 1.6°。当转速为 100 rpm 时,相当于要在 5 ms 时间内将惯量为 $J=1.8 \times 10^4 \text{ g} \cdot \text{cm}^2$ 的转子组件启动。根据启动力矩 $M \approx 2\pi^2 J (N/60)^2 \times \text{减速比}$ 的关系,电机应有 $7.2 \times 10^3 \text{ g} \cdot \text{cm}$ 的力矩,这大大超出了 TDB-500 电机的力矩输出能力。为此,选择了变频方案。在电机电源电压不变的情况下,电源频率降低,定子电流增加,启动力矩上升,转子惯性力矩按平方规律下降。图 3 表明,转速约在 25 rpm 时,电机的启动力矩与惯性力矩相等。转子组件的摩擦力矩为 150 g·cm,电机在 45 V 电源电压时的最大整步力矩为 900 g·cm,变频起动的起始转速在 10 rpm,由图 3 可知,电机的启动力矩裕度为 9,运行力矩裕度为 5,保证了电机运行的可靠性。为解决电机的宽变频调速启动,研制了数字分相变频电源。

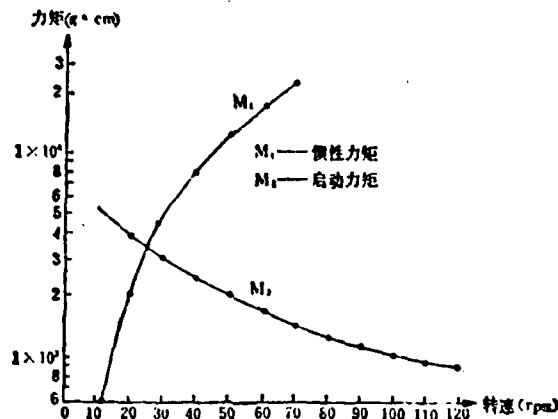


图 3 扫描镜组件的启动特性

4. 转动部件在超高真空中的润滑

在七百公里轨道以上,卫星空间环境的真空度高于 10^{-8} Torr。对于光机扫描系统来说,产生了在超高真空条件下的转动部件的润滑及运行寿命问题。

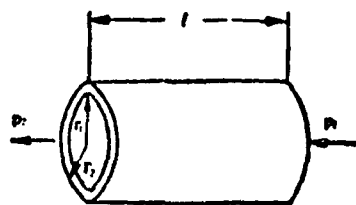


图 4 环形管道

常用的空间润滑方式有固体润滑和油气润滑两类。根据国外介绍和国内现有的条件,我们选用了储油轴承保持架和转轴出轴部分迷宫密封的油气润滑结构方案,并对此方案进行了地面高真空长寿命运行试验。

分析图 4 的环状管道,以 r_1 表示转轴的内径, r_2 表示轴孔的外径,在气体分子的平均自由程 λ 远大于轴半径 r_1 时,环形管道的气导 F 为:

$$F = 80.48 \sqrt{\frac{T}{M}} \frac{(r_2^2 - r_1^2)(r_2 - r_1)}{l}, [l/s] \quad (5)$$

其中, T 是绝对温度, M 是气体克分子量, l 是管道长度。

环形管道中的气体流量 U 为:

$$I' = (P_1 - P_2)F, [\text{Torr} \cdot \text{L} \cdot \text{s}], \quad (6)$$

其中, $P_1 - P_2$ 是环形管道两边的压力差。

由上式知道, 从环形管道中逸出的气体流量与压差及气导有关。在外层空间, $P_2 \approx 0$, 所以环形管道两边的压差主要取决于转动装置内部的气体压力。根据上面分析, 只要选择低饱和蒸气压的润滑油, 控制转动轴的出轴间隙和长度, 在电机储油器及轴承保持架内存有足够的润滑油, 是可以使电机内部长期保持润滑油的饱和蒸气压, 达到轴承润滑的目的。

我们选用 114[#] 硅油作润滑剂, 它的克分子量为 8047, 50°C 时的饱和蒸气压为 1×10^{-7} Torr, 迷宫间隙尺寸 $r_2 = 1.1 \text{ cm}$, $r_1 = 1.095 \text{ cm}$, $l = 1 \text{ cm}$, 由上面公式计算得到, 从两个迷宫出口一年时间向外层空间逸出的润滑油总量为 1 mg。如果在扫描器内储油 100 mg, 就足以保证扫描器在轨道上连续运行两年的需要。

为了验证上述方案, 我们将扫描组件放在 KM-0.5 容器中, 用无油的 2TL-500 型喷射钛离子泵抽至 $3 \sim 6 \times 10^{-7}$ Torr, 进行模拟试验。扫描器以 120 rpm 的转速连续运行半年, 没有发现轴承摩擦力矩有明显变化。

5. 飞行中的辐射定标

为了从红外扫描仪的输出信号推断目标辐射强度和目标的温度, 需要对扫描仪进行辐射定标。

在外层空间存在着温度为 3 K 的冷空间背景, 它在 $10.5 \sim 12.5 \mu\text{m}$ 中的辐射出射度仅为常温目标辐射的 $1/10^{22}$, 可以作为扫描仪的零辐射参考基准。红外通道碲镉汞探测器的输出信号幅值为微伏量级, 为避免弱信号放大过程中的直流漂移, 红外前置放大器采用交流耦合。由于耦合电容隔去了信号中的直流分量, 前置放大器的输出只反映接收辐射的变化。为测量其绝对强度, 在扫描仪看到冷空间时, 逻辑控制电路产生一个直流恢复脉冲, 使恢复放大器的直流恢复电容 C , 经导通二极管 D 迅速对地放电, 建立与空间零辐射相对应的零信号电平 (见图 5)。在直流恢复脉冲过后, 二极管断开。若 $RC > \frac{1}{\omega_L}$ (ω_L 是通道放大器的下限频率), 电容 C 就起到零电平箝位作用, 随后的输出信号幅度 V_L 与扫描仪接收的目标绝对辐射强度成正比。

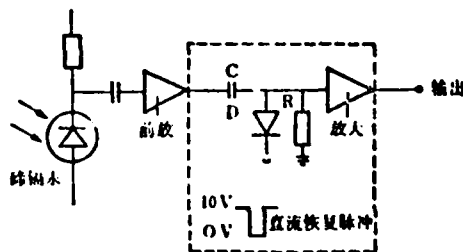


图5 直流恢复放大器原理图

$$V_L = \frac{1}{\pi} K \Omega A \int_{\lambda_1}^{\lambda_2} \mathcal{E}(\lambda) \tau_0(\lambda) P(\lambda, T_u) d\lambda, \quad (7)$$

$$P(\lambda, T_u) = \frac{C_1}{\lambda^5 (\exp \frac{C_2}{\lambda T_u} - 1)},$$

其中, T_u 为目标温度, $C_1 = 3.74 \times 10^{-16} \text{ W} \cdot \text{cm}^2$, $C_2 = 1.438 \text{ cm} \cdot \text{K}$, $\tau_0(\lambda)$ 为光学效率, $\mathcal{E}(\lambda)$ 为探测器响应率, A 为光学系统辐射接收面积, Ω 为瞬时视场, K 为电子学放大倍数。

为了测定信号 I' 所对应的目标辐射绝对强度, 在仪器中引入一个参考黑体 (例如, 可将仪器壳体做成参考黑体), 设扫描仪看到参考黑体时的输出信号为 I_s , 于是:

$$I_s = \frac{1}{\pi} K \Omega A \int_{\lambda_1}^{\lambda_2} \mathcal{E}(\lambda) \tau_0(\lambda) P(\lambda, T_s) d\lambda, \quad (8)$$

(6)

其中 T_s 为参考黑体的温度。于是:

$$\frac{V_1}{V_2} = \frac{\int_0^\infty \mathcal{R}(\lambda) \tau_0(\lambda) P(\lambda, T_s) d\lambda}{\int_0^\infty \mathcal{R}(\lambda) \tau_0(\lambda) P(\lambda, T_s) d\lambda} \quad (9)$$

上式中信号 V_1 和 V_2 的比值可在地面测出, T_s 可通过参考黑体温度测温获得, 因此, 通过上式就可以反演出目标的等效黑体温度。

6. 地面辐射定标

探测器的响应率 $\mathcal{R}(\lambda)$ 可用精确控制辐射致冷器冷块温度使其保持不变, 但扫描仪的光学效率 $\tau_0(\lambda)$ 将随着仪器温度变化 (主要取决于分色片和滤光片)。参考黑体因吊上仪器的结构和重量限制, 它的黑度不能做得很高, 因此, 扫描仪在发射前应在地面进行辐射定标, 以便得到如下的一组定标曲线, 供用户使用 (见图 6)。

对带有辐射致冷器在内的扫描仪的红外通道的辐射定标, 必须在具有模拟冷背景的真

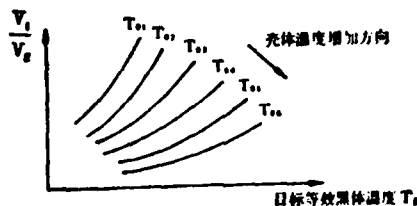


图 6 辐射计辐射定标曲线

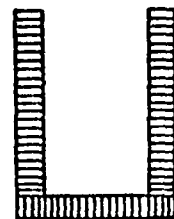


图 7 腔形蜂窝表面黑体

空系统内进行。冷背景温度应在 33 K 以下, 这时它对二级冷块致冷量的影响小于 1%。试验时, 将辐射致冷器对准冷屏, 用真空罐的液氮热沉 (一般为 90 K, 在 10.5~12.5 μm 内的辐射强度仅为 270 K 黑体目标的万分之一) 作为信号直流恢复时的零辐射参考基准。

定标时的标准黑体可用蜂窝面源, 面源尺寸应能充满扫描仪的通光口径及瞬时视场。根据文献的报道, 若铝制蜂窝的每一窝元的宽度为 6 mm, 长度为 25 mm, 壁厚为 0.05 mm, 表面喷涂热辐射效率为 $\epsilon = 0.95$ 的黑漆, 这时面源等效热辐射效率 $\epsilon_s = 0.996$ 。这相当于在 270 K 时与理想黑体有 0.23 K 的温差。

为了进一步提高面源黑体的热辐射效率, 可将蜂窝面源板做成腔体, 如图 7 所示, 腔体开口直径与长度之比应为 1:2。

按 Gouffe 公式, 估算腔体的等效热辐射效率 ϵ_s 为:

$$\epsilon_s = \frac{\epsilon_1(1+m)}{\epsilon_1(1-A/S) + A/S} \quad (10)$$

其中: 腔壁的等效热辐射效率 $\epsilon_1 = 0.996$, 开口面积与腔体表面积之比 $A/S = 1/12$,

$$m = (1 - \epsilon_1)(A/S - A/S_0) = 0.001 \left(\frac{1}{12} - \frac{1}{4\pi} \right) = 6 \times 10^{-3}$$

S_0 是直径等于腔体深度的球面积。于是可算得, $\epsilon_s = 0.99976$ 。这表明 270 K 时因热辐射效率带来的等效黑体温度误差小于 0.01 K。这时扫描仪的辐射定标的精度将由腔形面源黑体的温度误差, 及扫描仪输出信号的信噪比及信息处理方法决定。

参 考 文 献

- [1] Haviland E. P. and House, C. M., *Handbook of Satellites and Space Vehicles*, New York: D. Nostrand Comp. 1965.
- [2] Guthrie A., *Vacuum Technology*, New York: Wiley, 1963.
- [3] Baker M. L. and Minnison M. W., *An Introduction to Astrodynamics*, Academic Press, 1960.
- [4] *Advanced Very High Resolution Radiometer, Final Engineering Report*, NASA CR-156682, 1978.
- [5] *The TIROS N/NOAA A-G Satellite Series*, NES-95, 1978.
- [6] *ITOS Meteorological Satellite System, Final Engineering Report*, NASA CR-180163, 1973.
- [7] 小哈得兰, R. D., 红外系统原理, 国防工业出版社, 1975.
- [8] 朱子文, 微特电机, (1979), 第1期.

SEVERAL PROBLEMS IN DEVELOPING SATELLITE-BORNE INFRARED REMOTE SENSOR AND WAYS TO SOLVE THEM

KUNG HUIXING

(Shanghai Institute of Technical Physics, Academia Sinica)

ABSTRACT

Several specially-considered problems in developing a satellite-borne infrared remote sensor are discussed. These problems include: the definition of scanning period, the scanner and its lubrication in outer-space environment of very high vacuum, and infrared radiation calibration and so on. The ways to solve them are suggested.

領
大
情
定
誤

卫星
由于地面
大气温度
对一

这里, M
 $\tau(P)$ 为
温, T , 和
以往
把地面作
或者把 T
少对选用的。
陆地
光雷达直
大, 同时
定, 还影响
气温度反

本文 19

and Comp.

陆地上空大气温度的卫星红外遥感

赵高祥

(中国科学院大气物理研究所)

INE
LEMfrared re-
g period,
aum, and
i.

摘要——本文研究了 ϵ 和 T_s 对大气温度反演的影响,以及同时得出 ϵ 、 T_s 与大气温度的可能性。数值试验结果表明,在地面气压已知和当地面是灰体的情况下,若 ϵ 和 T_s 中有一个已知,我们就在得出大气温度的同时,精确地确定另一个地面参数;若 ϵ 和 T_s 都未知,也能把它们与大气温度一起很好地反演出来。

一、引言

卫星遥感能够提供全球(包括陆地和海洋)从地面到平流层顶之间的大气温度廓线。但由于地面的性质比海面复杂得多,地面的热辐射效率和地面温度不易预先确定,陆地上空的大气温度反演相应地也困难得多。

对一组卫星测温通道来说,第 i 个通道测到的向上辐射强度可表示为:

$$R_i = [\epsilon_i B_i(T_s) + (1 - \epsilon_i) \hat{R}_i] \tau_i(P_i) + \int_{\tau_i(P_i)}^1 B_i(T) d\tau_i(P), \quad (1)$$

($i = 1, 2, \dots, M$)

这里, M 为通道数, ϵ 为地面热辐射效率, B 为普朗克函数, \hat{R}_i 为有效向下天空辐射强度, $\tau(P)$ 为从气压 P 处到大气顶的透射率, 下标 i 表示第 i 个通道的量, T 是气压 P 处的气温, T_s 和 P_s 分别表示地面温度和地面气压。

以往从辐射传输方程式(1)解得大气温度廓线时,假定地面热辐射效率是已知的(通常把地面作为黑体,取 $\epsilon = 1$), P_s 取平均海平面(1013 hPa), T_s 由窗区通道测出,均作为已知量^[1-3];或者把 T_s 作为未知量,与大气温度一并求出^[4,5]。对于海面,其热辐射效率十分接近于1(至少对选用的一组测温通道,热辐射效率可以作为已知的常数),因此,上述处理方法是适用的。陆地情况则不同,虽然地面气压 P_s 可根据各地的地形高度定出,或者可在卫星上用激光雷达直接测出^[6],但热辐射效率随地表性质的不同而有明显变化,数值上可与1相差较大,同时它还随波长的不同而不同^[7-10],显然不是一个常数;地面热辐射效率无法正确确定,还影响到用窗区通道测定地面温度^[11-13],使推算得到的 T_s 产生误差。因此,陆地上的大气温度反演比海面更为困难,对非统计反演方法来说尤其如此。

本文1981年7月8日收到。

目前, 美国泰罗斯 N 系列卫星使用分区统计回归法作温度反演, 它把全地球分成纬度 60° 到极地和 30° 到 60° 各两个纬度带, 以及 30°S 到 30°N 一个纬度带, 共五个纬度带。然后求出各自的回归系数, 这些回归系数要根据无线电探空和卫星得到的一致资料不断地进行修正^[20]。另一方面, 人们正在研究不依赖于常规资料, 但所得精度可与使用常规资料的方法相比的反演方法。

文献 [17] 的作者利用文献 [4] 的反演方法研究了把非黑体地面当作黑体处理, 对地面温度和大气温度反演的影响, 数值试验中所取的地面热辐射效率, 在 $4.3\mu\text{m}$ 带为 0.85 和 0.95, 在 $15\mu\text{m}$ 带为 0.85 和 0.98。结果表明, 所造成的误差是不能忽略的。

本文研究 ϵ 和 T_s 对温度反演的影响, 并考察了将 ϵ 和 T_s 与大气温度一同求得之可能性。

二、数学处理

把测温通道选在 $15\mu\text{m CO}_2$ 带, 则式 (1) 右边的地面反射天空辐射项与地面发射项相比是一个小项, 因而用适当的模式来近似不会造成明显的误差。文献 [17] 得出, 有效向下天空辐射强度 R_{\downarrow} 可表示为:

$$R_{\downarrow} = F_s B_s(T_s)(1 - \tau_s(P_s)), \quad (2)$$

式中, 因子 F_s 可看作为一个只与通道有关的常数, 在不同的大气温度层结下, 它的差别很小, 因而可以预先用逐线计算法对一组遥感通道确定相应的一组常数 $[F_s]$ 。这样, 式 (1) 就可改写成:

$$R_i = [\epsilon_i + F_i(1 - \epsilon_i)(1 - \tau_i(P_s))] B_i(T_s) \tau_i(P_s) + \int_{\tau_{s0}}^1 B_i(T) d\tau_i(P), \quad (3)$$

假定地面气压 P_s 已知, 对选定的一组通道所在的波段, 地面可看作灰体 (即 $\epsilon_i = \epsilon$, $i = 1, 2, \dots, M$), 则由式 (3) 可以得到:

$$R_i = R_i^0 + \Delta R_i^0, \quad (4)$$

式中:

$$R_i^0 = [\epsilon^0 + F_i(1 - \epsilon^0)(1 - \tau_s^0)] B_i(T_s^0) \tau_s^0 + \int_{\tau_{s0}}^1 B_i(T^0) d\tau_i^0(P), \quad (5)$$

$$\begin{aligned} \Delta R_i^0 = R_i - R_i^0 = & [1 - F_i(1 - \tau_s^0)] B_i(T_s^0) \tau_s^0 \Delta \epsilon^0 \\ & + [\epsilon^0 + F_i(1 - \epsilon^0)(1 - \tau_s^0)] \tau_s^0 \frac{\partial B_i(T_s)}{\partial T_s} \bigg|_{T_s^0} \Delta T_s^0 \\ & + \int_{\tau_{s0}}^1 \frac{\partial B_i(T)}{\partial T} \bigg|_{T^0} \Delta T^0 d\tau_i^0(P), \end{aligned} \quad (6)$$

在式 (5) 和式 (6) 中, $\tau_s^0 = \tau_s(P_s)$ (下同)。将地面以上的整个大气层分成 N 个薄层, 应用数值积分公式, 式 (6) 可表示为:

$$\Delta R_i^0 = R_i - R_i^0 = \sum_{j=1}^{N+1} A_{ij}^0 \Delta X_j^0, \quad (i = 1, 2, \dots, M) \quad (7)$$

式中,

$$A_{ij}^0 = \frac{\partial B_i(T)}{\partial T} \bigg|_{T^0} [\tau_i^0(P_{j-1}) - \tau_i^0(P_j)], \quad (j = 1, 2, \dots, N)$$

$$A_{i,N+1}^0 = [\epsilon^0 + F_i(1 - \epsilon^0)(1 - \tau_s^0)] \tau_s^0 \frac{\partial B_i(T_s)}{\partial T_s} \bigg|_{T_s^0} \Delta T_s^0$$

$P_s = 0$, $\tau_s(P_s)$ 式的解;

式 (8) 中的 I 值的量。迭代

时终止, ϵ 为:

我们用了
测量误差为
列几种不同

序 号	注
第一组	
第二组	

1. ϵ 和
2. 假设
3. $\epsilon \in$
4. ϵ 为
5. $\Delta T_s^0 = 0$, 且
6. ϵ 为
- 在各
- 三十七个日
- 假偏差 ($^\circ\text{C}$)
- 从表
- 面上空大
- 面参数 ϵ 的
- 的一个时,
- 知时 得
- 0.15 ($^\circ\text{C}$)。

球分成纬度
带。然
资料不断地
用常规资料

理, 对地面
为 0.85 和

得之可能

反射项相比
向下天空

(2)

的差别很
小, 式(1)就

(3)

, $i=1, 2,$

(4)

(5)

(6)

, 应用数

(7)

$$A_{ij}^{(n)} = [1 - F_i(1 - \tau_a^{(n)})] B_i(T_j^{(n)}) \tau_a^{(n)},$$

$$\begin{cases} \Delta X_j^{(n)} = \Delta T_j^{(n)}, & (j=1, 2, \dots, N), \\ \Delta X_{N+1}^{(n)} = \Delta T_{N+1}^{(n)}, \\ \Delta X_{N+2}^{(n)} = \Delta \epsilon^{(n)}, \end{cases}$$

$P_0=0, \tau_i(P_0)=1, T_j$ 为第 j 层大气的平均温度。利用文献[5]的方法, 式(7)可有矩阵形式的解:

$$\Delta \mathbf{X}^{(n)} = (\mathbf{A}^{(n)})^{-1} [\mathbf{A}^{(n)} (\mathbf{A}^{(n)})^{-1} + \mathbf{r} \mathbf{I}]^{-1} \Delta \mathbf{R}^{(n)}, \quad (8)$$

$$\mathbf{X}^{(n+1)} = \mathbf{X}^{(n)} + \Delta \mathbf{X}^{(n)}, \quad (9)$$

式(8)中的 \mathbf{I} 为 $M \times M$ 维单位矩阵, r 为光滑因子, 角码 l 表示迭代次数, $l=0$ 为相应于初值的量。迭代过程到

$$|\Delta R_i^{(n)}| < \epsilon, \quad (i=1, 2, \dots, M)$$

时终止, ϵ 为观测误差。

三、数值试验结果和讨论

我们用文献[5]中的两组三角形响应函数的通道(见表1), 在假定地面气压为 1000 mb, 测量误差为 $0.8 \text{ erg} \cdot \text{s}^{-1} \cdot \text{cm}^{-1} \cdot \text{ster}^{-1}$ 、地面热辐射效率在 0.8 到 0.99 之间变化, 以及在下列几种不同的地面条件下, 进行了温度反演的数值试验:

表1 两组测温通道之通道数和各通道中心频率

序 号	通道数	各 通 道 中 心 频 率 (cm^{-1})
第一组	7	668, 679.5, 692, 704.5, 717, 732, 747
第二组	17	668, 672, 677, 682, 687, 692, 697, 700.5, 702, 707, 712, 717, 722, 732, 747, 752, 757

1. ϵ 和 T_i 已知; 这时 $\Delta \epsilon^{(n)}=0, \Delta T_i^{(n)}=0$, 系数矩阵 $\mathbf{A}^{(n)}$ 退化为 $M \times N$ 维的矩阵。

2. 假定地面为黑体($\epsilon^{(n)}=1$), T_i 未知; 这时 $\Delta \epsilon^{(n)}=0$, 系数矩阵 $\mathbf{A}^{(n)}$ 为 $M \times (N+1)$ 维的矩阵。

3. ϵ 已知, T_i 未知; 这时 $\Delta \epsilon^{(n)}=0$, 系数矩阵 $\mathbf{A}^{(n)}$ 为 $M \times (N+1)$ 维的矩阵。

4. ϵ 未知, T_i 作为已知, 但假定与“真实”地面温度间有 0°C 、 2°C 和 5°C 之偏差; 这时 $\Delta T_i^{(n)}=0$, 系数矩阵 $\mathbf{A}^{(n)}$ 退化为 $M \times (N+1)$ 维的矩阵。

5. ϵ 和 T_i 都作为待求的未知数; 这时系数矩阵 $\mathbf{A}^{(n)}$ 为 $M \times (N+2)$ 维的矩阵。

在各种不同的地面条件下进行数值试验得到的结果列于表2, 包括: 从 10 mb 到地面共三十七个压力层上总的大气温度均方根偏差 $\text{RMS}(^\circ\text{C})$; 其中十九个层上和地面的温度均方根偏差 $(^\circ\text{C})$; 以及地面热辐射效率的均方根偏差 $\Delta \epsilon$ 。

从表2可以看到, 用十七个通道得到的结果明显地优于用七个通道得到的结果, 这与海面上空大气温度反演的结果一样^[2]。下面让我们考察用十七个测温通道得到的结果。在地面参数 ϵ 和 T_i 都精确知道的情况下, 大气温度反演的结果最好, 但是, 在只知道 ϵ 和 T_i 中的一个时, 我们也得到了同样好的结果, 而且同时能精确地得出另一个地面参数(在 T_i 已知时得到的热辐射效率的均方根偏差为 0.0022 ; 在 ϵ 已知时, 得到的 T_i 的均方根偏差为 0.15°C)。不过, 当已知的一个地面参数有误差时, 反演出的另一个地面参数也有误差, 同

• 102 •

(1) 有 \bullet 号的列是210次数值试验的结果,其余为289次数值试验的结果;

2) ϵ 和 T_s 分别为地面热辐射效率和地面温度, ϵ' 和 T_s' 分别为假定已知的地面热辐射效率和地面温度。

(2) ϵ 和 T_s 分别为地面热辐射效率和地面温度, ϵ' 和 T_s' 分别为假定已知的地面热辐射效率和地面温度。

时,会使大
从表 2
相当,而且
是以一个倍
 T_0 、 ϵ 未知
近地面的月
在精
面参数 ϵ 有
况有差别,
大气温度
成比例的。
度上能相
是地面参
得出大气
我们
情况下,第
 T_0 。在这
否而决定
参数的信
度反演中,
上就有负
对地面透
参数的方
参数的信
存在,则在
以补偿,最
结果就说
表 2
表示)得
小,只是在
1.79°C 和
反射天空
反演造成
在地
mb 时的
(a)是一
由于
度反演时
。但从

1) 有“号”列是210次数值试验的结果,其余为289次数值试验的结果;
2) ϵ 和 T_s 分别为地面热辐射效率和地面温度, ϵ 和 T_s 分别为假定已知的光谱辐射效率和地面温度。

0.0023	0	0.0237	0	0.0697	0.0232	0.0022	0	0.0022	0	0.0023
--------	---	--------	---	--------	--------	--------	---	--------	---	--------

时,会使大气温度反演的误差增大,这种影响主要发生于接近地面的一些层上,

从表2还可看出,当 T_s 和 ϵ 都未知时,大气温度的反演精度也与 T_s 和 ϵ 已知情况下相当,而且同时能精确地求出 T_s 和 ϵ (两者的均方根偏差分别为 1.13°C 和 0.0155)。图1是以一个模式大气和两个无线电探空的温度廓线作为“真实”情况时,分别用 T_s 、 ϵ 已知和 T_s 、 ϵ 未知的两种不同地面条件进行反演的结果的比较。两种条件下的反演结果只是在接近地面的层上有一些小的差别,再往上去,两者几乎完全相同。

在精确知道地面对出射辐射的贡献时,地面参数对大气温度反演是没有影响的。当地面参数 ϵ 和 T_s 已知时,就近似于这种情况,在其他情况下,大气温度的反演结果与上述情况有差别,这个差别主要是由地面参数的误差造成的。但是,相对来说,地面参数的误差对大气温度差别的影响并不显著,而从表2可见,在 ϵ 和 T_s 之间,它们的误差的影响是接近于成比例的。式(5)中地面的贡献主要来自地面发射项,这也意味着 ϵ 和 T_s 的作用在很大程度上能相互补偿,说明在两个地面参数之间有着比它们与大气温度之间更密切的关系。正是地面参数和大气温度之间的这种既有内在联系,又有相对独立性的关系,使我们有可能在得出大气温度的同时,很好地确定地面参数。

我们知道,大气影响经订正后,可由一个窗区通道在地面参数 ϵ 和 T_s 中有一个已知情况下,把另一个确定下来。在有两个热辐射效率相同的窗区通道时,可以同时确定 ϵ 和 T_s 。在这类情况下,不考虑其他误差,得出的地面参数的误差是由对大气影响的订正正确与否而决定的。在我们所用的测温通道中,那些地面透射率不等于零的通道也都包含着地面参数的信息,只是这些通道处在吸收带,大气影响很大,要作订正就更困难。不过,由于在温度反演中,得到的温度廓线与实际廓线相比,往往在一些层上有正偏差时,在相邻的一些层上就有负偏差,从而整层大气的贡献(式(3)右端的最后一项)仍可能接近于实际值。同时,对地面透射率来说,大气温度层结不同的影响是不太大的;这样,由式(3)可以得出关于地面参数的方程,有可能象在窗区那样把 ϵ 和 T_s 确定下来。但是,这些通道所包含的关于地面参数的信息量比在窗区情况下小,而大气影响订正的误差则可能较大;再考虑到观测误差的存在,则在同样的通道数目下,不可能象在窗区情况下那样好地确定地面参数。为了对此加以补偿,就需要采用更多的包含地面和大气信息的通道,用十七通道比用七通道取得更好的结果就说明了这一点。

表2的最后四列是在反演过程中用的一组系数 $[F_s]$ 比实际值小10%时(在表中用 F_s' 表示)得到的结果。可以看出,它们与相应条件下用正确的系数 $[F_s]$ 所得到的结果差别很小,只是在 ϵ 和 T_s 都未知时,反演得到的地面温度和热辐射效率有稍大的误差(分别为 1.79°C 和 0.0237),但即使在这种情况下,对大气温度反演的影响也不大。这说明由于地面反射天空辐射项与地面发射项相比是小项,因而在计算系数 $[F_s]$ 中有一些误差将不至于对反演造成严重的影响,这一点对实际应用来说是有利的。

在地面气压为其他值的情况下,也可以得到类似的结果,图2为在地面气压 $P_s=700\text{mb}$ 时的结果。可以看出,在地面参数 ϵ 和 T_s 未知的情况下,仍可以得到很好的结果(图2(a)是一个个例,图2(b)是289次数值试验得到的 10mb 以下各层上的温度均方根偏差)。

由于地面情况随地点和季节而变化,地面热辐射效率又随波长而变化,因此要在大气温度反演时预先用其他手段把地面参数 ϵ 和 T_s 正确地确定下来,本身就是一个十分困难的问题。但从上面的结果看,当选用的一组测温通道所在的光谱区域中(实际上只要在地面透射

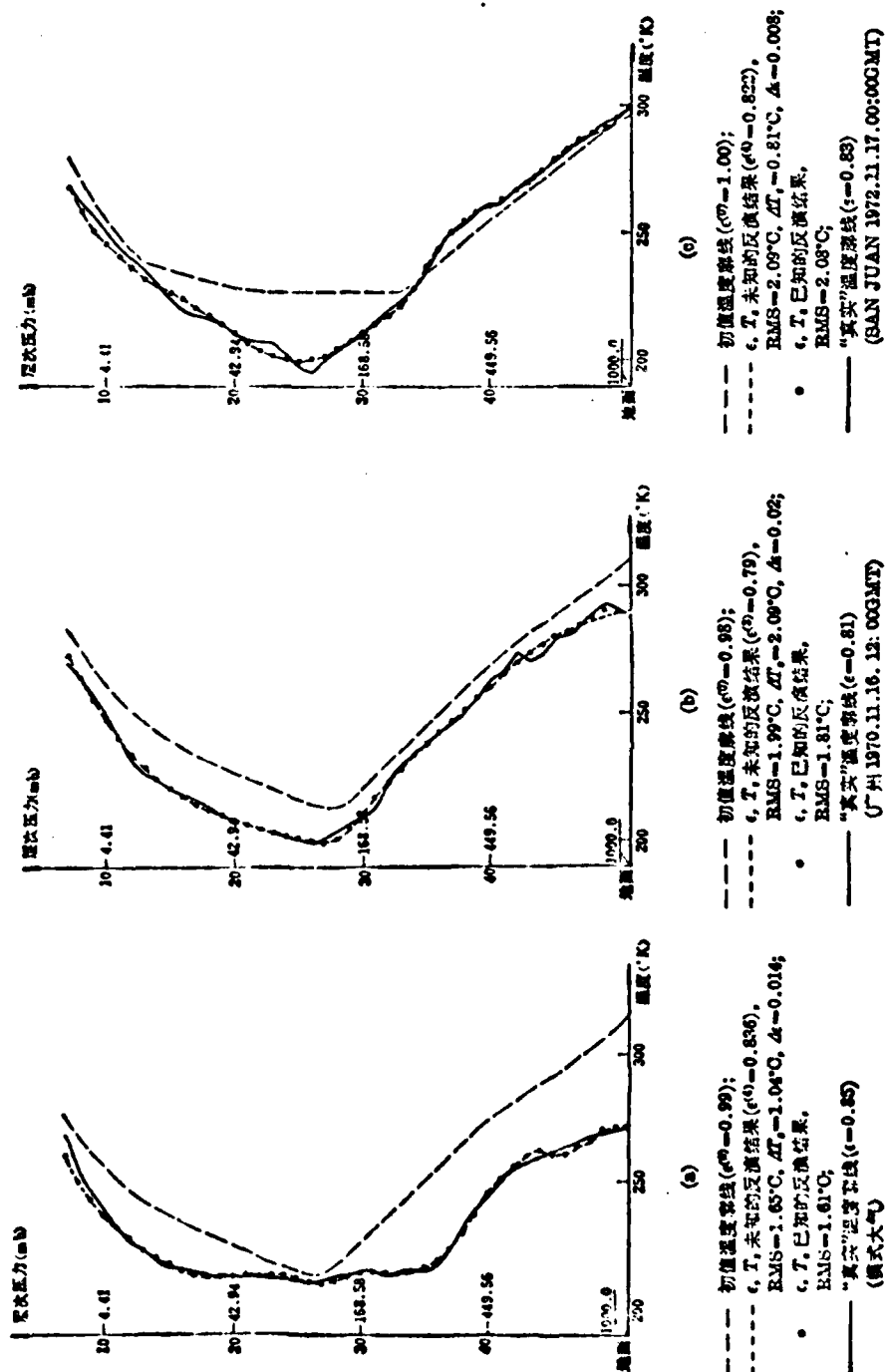


图1 反演结果与“真”温度廓线的比较

率不为零的几个通
 先得到关于地面参
 很好地得出,这是十

致谢——本文承周:

- [1] 曾庆存, 大气红外
- [2] 袁重光 and 曾庆存,
- [3] Wark D. Q. and
- [4] Obahine M. T., J
- [5] 赵高祥, 科学通报,
- [6] Singer R. F., 4p
- [7] Buettner K. J. a
- [8] Vincent E. K. et
- [9] Griggs M., J. Ge

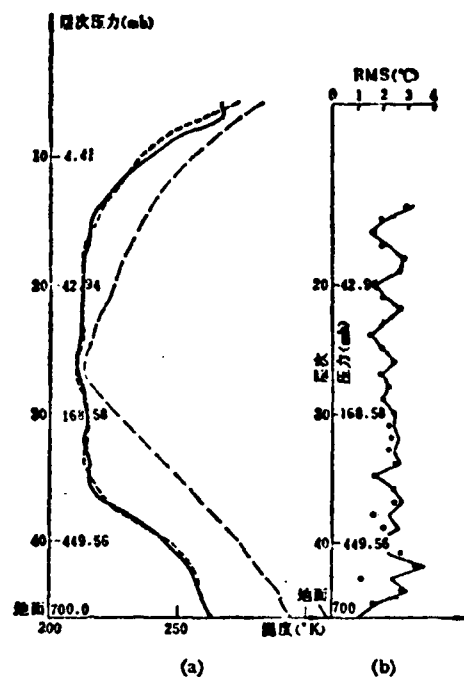


图2 地面气压 $P_g=700$ mb 时的温度反演结果

- (a) --- 初值温度廓线 ($\epsilon^0=0.99$);
 ϵ, T_g 未知的反演结果,
 ($\epsilon^0=0.852$), $RMS=1.33^\circ C$, $\Delta T_g=0.18^\circ C$, $\Delta \epsilon=0.002$;
 —— “真实”温度廓线 ($\epsilon=0.85$), 地面气压 $P_g=700$ mb.
 (b) 实线是 ϵ, T_g 未加时的结果, 总的均方根偏差为 $2.19^\circ C$,
 $\Delta \epsilon=0.0139$, $\Delta T_g=1.03^\circ C$
 圆点 (o) 为 ϵ, T_g 已知时的结果, 总的均方根偏差为 $2.10^\circ C$.

率不为零的几个通道所在的范围内), 可以把地面看作灰体时, 就不需要用另外的手段去预先得到关于地面参数 ϵ 和 T_g 的知识, 而可直接由这些测温通道把大气温度和地面参数同时很好地得出, 这是十分有意义的。

致谢——本文承周秀骥同志审阅并提出宝贵的意见, 特此致谢。

参 考 文 献

- [1] 曾庆存, 大气红外遥感原理, 科学出版社, 1974.
- [2] 袁耀光 and 曾庆存, 气象卫星的红外遥感及反演(一), 科学出版社, 1977, 19.
- [3] Wark D. Q. and Fleming, H. E. *Mon. Weather. Rev.*, 94 (1966), 6, 351.
- [4] Chahine M. T., *J. Opt. Soc. Am.*, 58 (1968), 12, 1634.
- [5] 赵高祥, 科学通报, 25 (1980), 23, 1079.
- [6] Singer S. F., *Appl. Opt.*, 7 (1968), 6, 1125.
- [7] Boettner K. J. and Kern, C. D. *J. Geophys. Res.*, 70 (1965), 6, 1339.
- [8] Vincent R. K. et al., *Remote Sens. Environ.*, 4 (1975), 3, 199.
- [9] Griggs M., *J. Geophys. Res.*, 73 (1968), 24, 7515.

- [10] Hovis W. A. Jr. et al., *Appl. Opt.*, **7** (1968), 6, 1137.
 [11] Weim M., *Appl. Opt.*, **10** (1971), 6, 1280.
 [12] Loreus D., *Appl. Opt.*, **7** (1968), 9, 1703.
 [13] Sutherland R. A. et al., *J. Appl. Meteorol.*, **18** (1979), 6, 1163.
 [14] Hovis W. A. Jr., *Appl. Opt.*, **5** (1966), 5, 815.
 [15] Shaw J. H., *J. Atmos. Sci.*, **27** (1970), 6, 950.
 [16] Phillips N. et al., *Bull. Amer. Meteorol. Soc.*, **60** (1979), 10, 1153.
 [17] Kornfeld and J. Susskind, *J. Mon. Weather. Rev.*, **105** (1977), 12, 1635.

1(1982), 2, 107~

迭层

INFRARED REMOTE SENSING OF OVER-LAND ATMOSPHERIC TEMPERATURE PROFILES FROM SATELLITE

ZHAO GAOXIANG

(Institute of Atmospheric Physics, Academia Sinica)

ABSTRACT

The effects of the surface parameters, ϵ and T_s , on atmospheric temperature retrieval, and the possibility of recovering simultaneously both ϵ , T_s and atmospheric temperature profiles are studied. The results of numerical simulations show that, when one of the two surface parameters is known, atmospheric temperature profiles can be derived and at the same time the other surface parameter can be determined accurately; and even if both ϵ and T_s are unknown, atmospheric temperature profiles and the two parameters can still be recovered with good accuracies.

摘要——
时间变化
效的。

在金属外壳
陷及其形状，
是，当外壳较厚，
被检试样表面各
2 mm 厚锰钢和

本研究采用
1. 单层均
取试样表面
间，试样可以看
流从试样表面注
为试样中热流是

其中，

本文 1982 年 11 月

整好被
 用状态,

由卫星测值计算短波红外大气窗区 亮度温度的一种方法

汪 勤 模

(中央气象局卫星气象中心)

摘要——本文提出了利用 $3.7\mu\text{m}\sim 4.0\mu\text{m}$ 大气窗区内两个通道的同时测值和多项式拟合法计算短波红外大气窗区亮度温度的一种公式。计算误差小于 $\pm 0.4\text{K}$ 。概述了利用这个亮度温度对 $4.3\mu\text{m CO}_2$ 吸收带通道测值进行反射太阳辐射订正的方法。

图 5

一、引言

美国泰罗斯-N(TIROS-N)气象卫星上的改型高分辨率红外探测仪(HIRS/2)有两个位于短波红外大气窗区 ($3.7\mu\text{m}\sim 4.0\mu\text{m}$) 的通道,即 HIRS/2-18 和 HIRS/2-19,其中心波数分别是 2511.95cm^{-1} 和 2671.18cm^{-1} ,并记为 W_1 和 W_2 。利用这两个通道的同时测值,可以计算地球表面的反射率,估计由地球表面反射的太阳辐射对 $4.3\mu\text{m CO}_2$ 吸收带温度探测通道的影响。

二、计算方法

短波红外大气窗区对水汽的响应比长波红外大气窗区 ($11.0\mu\text{m}$) 弱得多,所以不象后者那样,水汽吸收是首要考虑的因子。然而,由地球表面反射的外来辐射是必须要考虑的,其中对大气向下辐射的反射分量不到地球表面辐射的百分之一,可以忽略不计。但是,反射的太阳辐射却占七分之一左右,乃是白天短波红外遥感中起主要影响的因子^[1]。

对于短波红外大气窗区,在无云大气条件下,辐射传递方程可简化为^[2]:

$$R(W) = \epsilon_s B(W, T_s) + \gamma_s J_0(W) \mu_0 \quad (1)$$

其中, $R(W)$ 是红外探测仪中短波红外大气窗区通道(中心波数以 W 示之)对着地球时测得的辐射强度。右边第一项是地球表面发射的辐射对 $R(W)$ 的贡献部分,第二项是地球表面反射的太阳辐射对 $R(W)$ 的贡献部分。 γ_s 和 ϵ_s 分别是地球表面的反射率和热辐射效率。 μ_0 是太阳天顶角 θ_0 的余弦,当 θ_0 大于 90° 时,就令 $\mu_0 = 0$ 。 $B(\nu, T')$ 是温度为 T' 的黑体在波数 ν 处的分谱辐射强度,亦称普朗克函数,

本文 1981 年 7 月 18 日收到。修改稿 1982 年 2 月 14 日收到。

$$B(\nu, T) = \frac{c_1 \nu^3}{\exp(c_2 \nu / T) - 1}$$

其中, c_1 , c_2 分别代表第一、第二辐射常数, $c_1 = 2hc^2$, $c_2 = hc/k$ 。

I_0 是到达地球表面的太阳辐射强度, 它近似表示为:

$$I_0(W) = B(W, T_{sun}) \frac{\Omega_{sun}}{\pi}, \quad (2a)$$

其中, T_{sun} 是太阳的亮度温度, 通常取为 5800~6000 K, Ω_{sun} 是太阳对地球所张的立体角, 是个常数, 约为 7×10^{-5} sr。在此我们假定太阳的直接辐射在量值上等于温度为 T_{sun} 的黑体辐射强度。

若计入大气气体成分对短波红外窗区太阳辐射的微量吸收效应, 方程(2a)改为:

$$I_0(W) = B(W, T_{sun}) \frac{\Omega_{sun}}{\pi} \tau^{(\sec \theta_0 + \sec \theta)}(W), \quad (2b)$$

其中 $\tau(W)$ 是局地垂直方向上的透过率, θ_0 是太阳天顶角, θ 是卫星天顶角。这样表示后, 方程(1)型式保持不变。

引用 Smith 关于在 $3.7 \mu m$ 至 $4.2 \mu m$ 这个狭窄的短波红外谱区内, γ_0 和 s_0 与波长近似无关的假定^[2], 根据方程(1)和(2), 得:

$$\frac{R(W_2) - \epsilon_0 B(W_2, T_b)}{R(W_1) - \epsilon_0 B(W_1, T_b)} = \frac{B(W_2, T_{sun})}{B(W_1, T_{sun})} \quad (3)$$

若取 $T_{sun} = 5800$ K, 对于 TIROS-N 的 HIRS/2-18 和 HIRS/2-19, 方程(3)右边为:

$$\frac{B(W_2, T_{sun})}{B(W_1, T_{sun})} = K = 1.10635. \quad (4)$$

按定义, 亮度温度 T_b 满足下式:

$$\epsilon_0 B(W, T_b) = B(W, T_b). \quad (5)$$

方程(3)可写为:

$$B(W_2, T_b) - KB(W_1, T_b) = R(W_2) - KR(W_1). \quad (6)$$

方程(6)是关于 T_b 的超越方程, 我们用多项式拟合法来建立 T_b 和辐射测值 $R(W_1)$ 和 $R(W_2)$ 之间的显式关系式。令:

$$f = R(W_2) - KR(W_1), \quad (7)$$

我们取三次多项式, 即:

$$T_b = \sum_{i=0}^3 a_i [\ln(-f)]^i, \quad (8)$$

由方程(6)和(7)可见, 我们可先计算出系数 a_i 。选取从 200 K 到 340 K (相当于世界上两个极端温度) 这样的温度范围, 就 TIROS-N 两个短波红外大气窗区通道, 使用最小二乘法, 建立关于 a_i 的线性方程组, 采用主元素消去法解该方程组, 计算结果如表 1 所示。

表 1 TIROS-N 上的 HIRS/2 短波红外窗区亮度温度计算的系数

a_0	a_1	a_2	a_3
811.0964	29.1788	2.5258	0.1266

这样, 根据 TIROS-N 上的 HIRS/2 通道 18 和 19 的同时测值, 按方程(7)计算 f , 然后代入方程(8)就得出 T_b , 其误差小于 ± 0.4 K (见表 2)。

表 3 多项式拟合法计算值(T_B)和模拟值(T)

$T(K)$	210	240	260	280	300	320	340
$T_B(K)$	210.08	239.95	259.86	279.97	300.13	320.09	339.68
$T_B - T$	0.08	-0.05	-0.14	-0.03	0.12	0.09	-0.32

须指出, 尽管在短波红外大气窗区, 水汽和其他气体成分影响相对较小, 但仍须考虑它们对测值的影响, 特别是在大气低层水汽含量相对较大时(本文假定在应用方程(8)之前已经对测值作了这些成分吸收的订正处理)。

三、地球表面反射率和反射太阳辐射项订正

利用卫星红外探测器短波红外大气窗区通道的测值计算出亮度温度 T_B 之后, 按方程(1), 反射率 γ_0 为:

$$\gamma_0 = \frac{R(W) - B(W, T_B)}{I_0(W)\mu_0},$$

若取 W 为 W_1 , 利用方程(2b)得:

$$\gamma_0 = \frac{R(W_1) - B(W_1, T_B)}{B(W_1, T_{sun})} \left[\frac{\Omega_{sun}}{\pi} \mu_0 \right]^{-1} [\tau^{sec \theta_0 + sec \theta}(W)]^{-1}. \quad (9)$$

位于 $4.3 \mu m$ CO_2 吸收带内某个通道(中心波数以 ν 示之)的反射太阳辐射订正项 $SO(\nu)$, 实际上就是方程(1)右边的第二项。

$$SO(\nu) = \frac{R(W_1) - B(W_1, T_B)}{B(W_1, T_{sun})/B(\nu, T_{sun})} \left[\frac{\tau(\nu)}{\tau(W_1)} \right]^{sec \theta_0 + sec \theta}, \quad (10)$$

其中, 太阳天顶角 θ_0 可利用卫星观测瞬间的地方时按天文学公式计算出来。还有一个参数——透射率, 须事先利用适当的方法求出。

参 考 文 献

- [1] 曾庆存, 大气红外遥测原理, 科学出版社, 1974.
- [2] Smith W. L. et al., NOAA TM NESS 57, 1974.
- [3] Smith W. L., WMO/UN Regional Training Seminar on the Interpretation, Analysis and Use of Meteorological Satellite Data, Tokyo, Japan, 23 Oct. to 2 Nov., 1978.

A METHOD OF DETERMINING THE BRIGHTNESS TEMPERATURE IN SHORT-WAVE IR ATMOSPHERIC SPECTRAL WINDOW FROM SATELLITE MEASUREMENT

WANG QINMO

(Satellite Meteorological Center, CKB)

ABSTRACT

Presented in this paper is a formula of calculating brightness temperature in short-wave IR atmospheric window from instantaneous radiance measurements of two channels in $3.7\sim 4.0\mu\text{m}$ spectral band by polynomial fit technique. Its accuracy is within $\pm 0.4\text{ K}$. The approach for determining corrections of reflected solar radiance on measurements in $4.3\mu\text{m}$ CO_2 absorption band is briefly described.

END

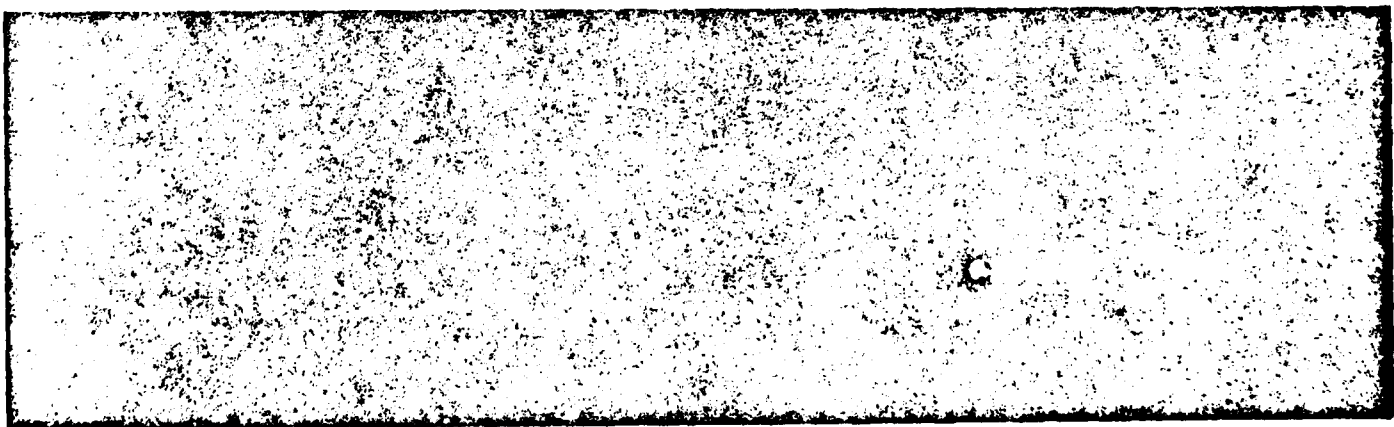
FILMED

3-18-83



FTD

RAC



END

FILMED

2-85

DTIC